



## Research Paper

Degradation of diclofenac in water under LED irradiation using combined g-C<sub>3</sub>N<sub>4</sub>/NH<sub>2</sub>-MIL-125 photocatalystsV. Muelas-Ramos<sup>a,\*</sup>, M.J. Sampaio<sup>b,\*</sup>, C.G. Silva<sup>b</sup>, J. Bedia<sup>a</sup>, J.J. Rodriguez<sup>a</sup>, J.L. Faria<sup>b</sup>, C. Belver<sup>a</sup><sup>a</sup> Departamento de Ingeniería Química, Universidad Autónoma de Madrid, Campus Cantoblanco, E-28049 Madrid, Spain<sup>b</sup> Laboratory of Separation and Reaction Engineering – Laboratory of Catalysis and Materials (LSRE-LCM), Departamento de Engenharia Química, Faculdade de Engenharia, Universidade do Porto, Rua Dr. Roberto Frias s/n, 4200-465 Porto, Portugal

## ARTICLE INFO

Editor: Dr. L. Haizhou

## Keywords:

NH<sub>2</sub>-MIL-125g-C<sub>3</sub>N<sub>4</sub>

Photocatalysis

LEDs

Diclofenac degradation pathway

## ABSTRACT

This study reports the photocatalytic degradation of diclofenac by hybrid materials prepared by combination of graphitic carbon nitride (g-C<sub>3</sub>N<sub>4</sub>) and titanium-metal organic framework (NH<sub>2</sub>-MIL-125), in different mass proportions (MOF:C<sub>3</sub>N<sub>4</sub> of 25:75, 50:50 and 75:25). The hybrid materials were fully characterized, and their properties compared to those of the individual components, whose presence was confirmed by XRD. The porous structure was the result of the highly microporous character of the MOF and the non-porous one of g-C<sub>3</sub>N<sub>4</sub>. The band gap values were very close to that of MOF component. Photoluminescence measurements suggested an increase on the recombination rate associated to the presence of g-C<sub>3</sub>N<sub>4</sub>. Photodegradation tests of diclofenac (10 mg·L<sup>-1</sup>) were performed under UV LED irradiation at 384 nm. The hybrid materials showed higher photocatalytic activity than the individual components, suggesting the occurrence of some synergistic effect. The photocatalyst with a MOF:g-C<sub>3</sub>N<sub>4</sub> ratio of 50:50 yielded the highest conversion rate, allowing complete disappearance of diclofenac in 2 h. Experiments with scavengers showed that superoxide radicals and holes played a major role in the photocatalytic process photodegradation, being that of hydroxyl radicals less significant. From the identification of by-products species, a degradation pathway was proposed for the degradation of diclofenac under the experimental operating conditions.

## 1. Introduction

The world's growing population and accelerated industrial development have notably increased wastewater effluents and their chemical complexity. This has been assessed thanks to the development of more powerful analytical techniques which enabled the identification of new pollutants, in many cases at very low concentrations (Jiménez et al., 2018). Emerging contaminants (ECs) are natural or synthetic chemicals with dangerous effects for human health and environment, which are categorized as pharmaceuticals and personal care products (PPCPs), veterinary products, pesticides, food additives and a wide diversity of industrial by-products. These compounds have shown to be recalcitrant to conventional treatments, despite founding in water in very low concentrations, resulting in their accumulation in water bodies. Nowadays, many studies are focused on the removal of these emerging contaminants from aqueous mediums (Ahmed and Jung, 2014; Arroyo and Molinos-Senante, 2018). Advanced Oxidation Processes (AOPs) are

considered very efficient methods that accelerate the oxidation of a wide variety of organic and inorganic pollutants resistant to more conventional treatment methods. This technology is based on the in-situ generation of transitory species (mainly hydroxyl radicals) with a very high oxidation capacity, which can degrade the target pollutant and even completely mineralize it to CO<sub>2</sub> and H<sub>2</sub>O (Miklos et al., 2018). The term AOPs includes various of technologies, such as Fenton-like processes, ozonation, electrochemical processes, the use of ultrasound, microwaves and γ-irradiation or heterogeneous and homogeneous photocatalysis (Brillas, 2020; Kanakaraju et al., 2018). The heterogeneous photocatalysis is based on the excitation of an optical semiconductor upon irradiation with light of energy higher or equal than the catalyst bandgap. The pairs of photogenerated charges react with the species absorbed on the surface of the catalyst allowing the oxidation of the pollutant (Bahnmann, 2004). One of the most critical factors affecting the photocatalytic behavior is the light adsorption by the photocatalyst. Thus, different light sources, such as solar radiation, UV lamps, lasers

\* Corresponding authors.

E-mail addresses: [virginia.muelas@uam.es](mailto:virginia.muelas@uam.es) (V. Muelas-Ramos), [mjsampaio@fe.up.pt](mailto:mjsampaio@fe.up.pt) (M.J. Sampaio).<https://doi.org/10.1016/j.jhazmat.2021.126199>

Received 17 December 2020; Received in revised form 19 May 2021; Accepted 20 May 2021

Available online 24 May 2021

0304-3894/© 2021 The Authors.

Published by Elsevier B.V. This is an open access article under the CC BY-NC-ND license

<http://creativecommons.org/licenses/by-nc-nd/4.0/>.

and light-emitting diodes (LEDs) have been analyzed. LEDs have long service life, low energy consumption and provoke a lower temperature increase than other illumination sources (Song et al., 2016).

Many different semiconductors have been analyzed as photocatalysts for the abatement of water pollutants, searching for materials with a broad light absorption spectrum, low charge recombination rate and high chemical stability. Graphitic carbon nitride ( $g\text{-C}_3\text{N}_4$ ) is a relatively novel semiconductor tested in recent studies. It possesses a good physicochemical stability together with unique 2D and appealing electronic structure. Besides, it is active under visible light, non-toxic and unexpensive (Zeng et al., 2016; Zhao et al., 2015a, 2015b). In 2009, Wang et al. (2009a, 2009b) reported using this material as photocatalyst. This material can be synthesized from cheap precursors such as dicyanamide, urea and melamine. Unfortunately, it presents some drawbacks as photocatalyst, such as relatively low photocatalytic performance, due to fast electron-hole recombination, slow reaction kinetics and relatively low light absorbance (Cao et al., 2015; Wen et al., 2017). To overcome these limitations, the combination of  $g\text{-C}_3\text{N}_4$  with other semiconductors has been evaluated (Liang et al., 2019; Xiao et al., 2019; Zhang et al., 2019; Zhou et al., 2019). One of those possible semiconductors are metal organic frameworks (MOFs) (Li et al., 2019; Panneri et al., 2017; Wang et al., 2019a, 2019b), a family of porous crystalline materials that are assembled by the combination of an organic linker and a metal oxo-cluster (Bedia et al., 2019). MOFs have many applications in different fields including water treatment, due to their high surface area, semiconductor character and tunable properties (Wang et al., 2018). Ti-containing MOFs, such as  $\text{NH}_2\text{-MIL-125}$ , are being widely investigated as photocatalysts (Fu et al., 2016; Wang et al., 2015; Zhu et al., 2016), due to the well-known photocatalytic properties of titania. So far, only few studies have investigated the degradation of emerging contaminants (ECs) with MOFs and  $g\text{-C}_3\text{N}_4$  combinations. Panneri et al. (2017) used graphitic carbon nitride with ZIF-8 to degrade tetracycline. This compound was completely converted in 60 min, although 45% removal was due to adsorption. (Li et al., 2019) combined the same materials to remove tetracycline under visible light. The best result (75.1% conversion) was achieved with 40% of ZIF-8 at pH 8. However, the adsorption contribution was also very significant (36%). They also prepared a combination of  $g\text{-C}_3\text{N}_4$ , PDI (pyromellitic diimide) and  $\text{NH}_2\text{-MIL-53 (Fe)}$  to remove tetracycline and carbamazepine under LED white lamp, with some addition of  $\text{H}_2\text{O}_2$  (Li et al., 2019).  $\text{MIL-53 (Fe)}$ /urchin-like  $g\text{-C}_3\text{N}_4$  has been tested by Salimi et al. (2020) to remove cefixime under simulated visible light, achieving around 80% conversion. The combination of different semiconductors can enhance the charge mobility and reduce the recombination rate, which extent the charge life and therefore can yield more reactive species and improve the photocatalytic degradation. The novelty of the present study relies on the application of an efficient photocatalytic process using  $g\text{-C}_3\text{N}_4/\text{NH}_2\text{-MIL-125}$  hybrids with enhanced activity towards DCF degradation using a low-cost and energy-efficient light source.

In this study, hybrid photocatalysts with different proportions of  $g\text{-C}_3\text{N}_4$  and  $\text{NH}_2\text{-MIL-125(Ti)}$  were tested for the breakdown of diclofenac, as model emerging contaminant, using LEDs as the irradiation source. Diclofenac is among the most-consumed nonsteroidal anti-inflammatory drug substances. The worldwide use of this substance has generated a considerable market research interest, making it one of the most common pharmaceuticals currently detected in the environment (UNESCO/HELCOM, 2017). The challenge was to further improve the photocatalytic activity of both  $\text{NH}_2\text{-MIL-125}$  and  $g\text{-C}_3\text{N}_4$  through a convenient combination of both semiconductors. To the best of our knowledge, this is the first study analyzing this combination to photodegrade diclofenac under UV LEDs. Special attention has been paid on the degradation pathway of diclofenac, identifying the reaction by-products and the reactive species involved in the photocatalytic process.

## 2. Experimental

### 2.1. Synthesis of $\text{NH}_2\text{-MIL-125}$

$\text{NH}_2\text{-MIL-125}$  was synthesized following the procedure proposed by Martis et al. (2014). Briefly, 2-amino benzene dicarboxylic acid (6 mmol, Aldrich, 99%) was dissolved in N,N-dimethylformamide (25 mL, DMF, Aldrich,  $\geq 99.8\%$ ) and stirred for 5 min. Then, titanium isopropoxide (3 mmol, Aldrich,  $\geq 97\%$ ) was added dropwise and, finally, methanol solvent was also added (25 mL, Sigma-Aldrich, anhydrous 99.8%). After 30 min under stirring, the mixture was placed in a 65 mL Teflon-lined stainless steel autoclave and maintained at  $150\text{ }^\circ\text{C}$  for 16 h. The solid, separated by centrifugation, was washed three times (30 min each) with 100 mL of DMF and three additional times with 100 mL of methanol in the same conditions. Finally, a yellow solid was obtained after centrifugation and dried at  $60\text{ }^\circ\text{C}$  overnight. It was named  $\text{NH}_2\text{-MIL-125}$ .

### 2.2. Synthesis of $g\text{-C}_3\text{N}_4$

$g\text{-C}_3\text{N}_4$  was prepared by thermal decomposition of dicyandiamide, as described by Lima et al. (2017). The precursor was heated in a muffle furnace under static air atmosphere until  $450\text{ }^\circ\text{C}$  at a heating rate of  $2\text{ }^\circ\text{C min}^{-1}$ . After 2 h, the temperature was increased up to  $550\text{ }^\circ\text{C}$  at  $2\text{ }^\circ\text{C min}^{-1}$  and maintained for 4 h. The resulting yellow solid was washed with ultra-pure water (300 mL), filtered and dried overnight at  $100\text{ }^\circ\text{C}$ . It was denoted as  $g\text{-C}_3\text{N}_4$ .

### 2.3. Preparation of the $g\text{-C}_3\text{N}_4$ and $\text{NH}_2\text{-MIL-125}$ photocatalysts

The hybrid materials to be tested as photocatalysts were prepared according to the procedure previously described by Xu et al. (2017). In the case of the 50:50 (MOF: $g\text{-C}_3\text{N}_4$ ) material,  $\text{NH}_2\text{-MIL-125}$  (100 mg) was added to a suspension with 100 mg of  $g\text{-C}_3\text{N}_4$  in isopropanol (6.7 mL), to adjust a concentration of  $15\text{ g}\cdot\text{L}^{-1}$ . Thus, 300 and 33 mg of  $g\text{-C}_3\text{N}_4$  were dissolved in 20 and 2.2 mL of isopropanol to obtain 25:75 and 75:25 materials, respectively. The suspensions were subjected to ultrasonication for 30 min and, then, heated at  $60\text{ }^\circ\text{C}$  for 24 h under stirring until total solvent evaporation. Then, a yellow powder was recovered after crushing in a mortar. The samples were denoted with the mass proportion of  $g\text{-C}_3\text{N}_4$  in the mixture, namely, 75% $\text{C}_3\text{N}_4$ , 50% $\text{C}_3\text{N}_4$  and 25% $\text{C}_3\text{N}_4$ .

### 2.4. Characterization

X-ray powder diffraction (XRD) patterns were obtained in a Bruker D8 diffractometer with a Sol-X energy-dispersive detector in a scanning range of  $2\text{--}50^\circ$ , using a Cu K $\alpha$  source. Elemental analysis was performed using a LECO CHNS-932 equipment. The porous texture was characterized by  $\text{N}_2$  adsorption-desorption at  $-196\text{ }^\circ\text{C}$  in a TriStar 123 equipment (Micromeritics). Before adsorption, samples were degassed in vacuum at  $120\text{ }^\circ\text{C}$  for at least 6 h. The specific surface area ( $S_{\text{BET}}$ ) was calculated using the BET method (Brunauer et al., 1938). The t-plot method (Lippens and de Boer, 1965) was used to determine the non-microporous surface area ( $S_{\text{EXT}}$ ), the micropore surface ( $S_{\text{MP}}$ ) and the micropore volume ( $V_{\text{M}}$ ). Total pore volume ( $V_{\text{T}}$ ) was obtained by the nitrogen amount adsorbed at 0.99 relative pressure. UV-visible reflectance spectra of solid samples were recorded from 185 to 800 nm with a Shimadzu 2501PC equipment and  $\text{BaSO}_4$  as reference. The bandgap values were determined from those spectra considering the solids as indirect semiconductors (Kampouri et al., 2018) and using the Tauc Plot technique (Tauc, 1970; Zhu et al., 2016). X-ray photoelectron spectroscopy (XPS) was employed to determine its chemical composition, using a Thermo Scientific apparatus using Al K $\alpha$  radiation (1486.68 eV). The morphology was observed using a transmission electron microscope (TEM, JEM-3000 F). EDX mapping images were obtained with an

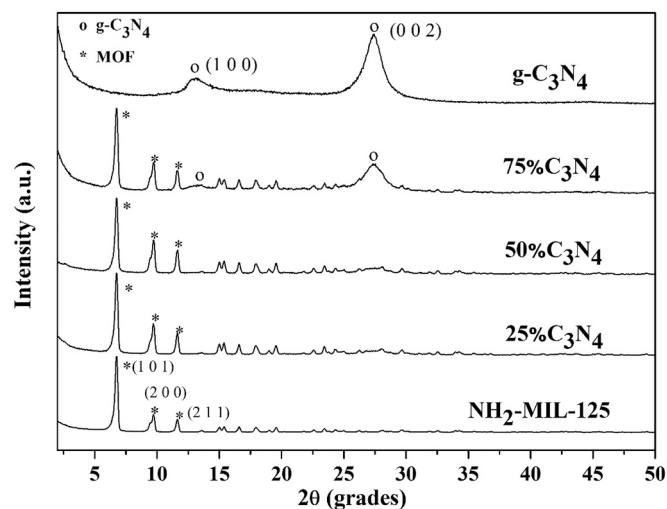


Fig. 1. XRD patterns of the bare semiconductors and the synthesized hybrid materials.

Analytical Titan apparatus (CEOSCo.) Photoluminescence spectra (PL) were obtained with a spectrofluorometer (Jasco FP-8300) with a 150 W Xenon lamp as light source. Analyses were conducted using both excitation and emission bandwidth fixed at 2.5 nm, with the excitation wavelength set at 370 nm.

## 2.5. Photocatalytic tests

Photodegradation of diclofenac (DCF, Aldrich, >99%) was performed in a borosilicate glass cylindrical reactor placed in a box with four LEDs (384 nm, the irradiation of each LED was 170 W·m<sup>-2</sup>). The photocatalyst (250 mg·L<sup>-1</sup>) was dispersed in an aqueous solution (100 mL) with a DCF initial concentration equal to 10 mg·L<sup>-1</sup>. Adsorption equilibrium was reached after 30 min in the dark. Subsequently, the photocatalytic reaction was maintained for 4 h. Samples were taken at given time intervals. The photocatalyst was removed by centrifugation and the liquid phase filtrated using PTFE syringeless filters (Whatman 0.2 μm). The experiments were performed by triplicate and the error bars were included. DCF was analysed by a Shimadzu Corporation Ultra High-Pressure Liquid Chromatography (UHPLC) apparatus. The chromatographic separation was carried out under isocratic mode by using a Kinetex™ XB-C18 100 Å column (100 × 2.1 mm i.d.; 1.7 μm particle diameter) supplied by Phenomenex, Inc. (Torrance, CA, USA) with a mobile phase composed of 0.1% formic acid aqueous solution and acetonitrile at 0.2 mL·min<sup>-1</sup>. Radical trapping experiments were carried out to check the main reactive species involved in the reaction with the most active photocatalyst. EDTA, TEMPO and tert-butanol (1 mM) were used as scavengers of holes, superoxide radicals and hydroxyl radicals, respectively. The by-products were detected by Liquid Chromatography Mass Spectrometry with electrospray ionization (LC/ESI-MS) in a Bruker Maxis II equipment using a positive ionization mode. The analyses were carried out with a 500 V end plate offset, at 200 °C, a 3.500 V capillary voltage and 6 mL·min<sup>-1</sup> of dry gas flow. The range of 50–3000 *m/z* was used to collect data. Ionic chromatography (IC) was carried out in a Metrohm 790 IC apparatus, equipped with a Metrosep A Supp 5 column, to quantify carboxylic acids and inorganic ions. Na<sub>2</sub>CO<sub>3</sub>/NaHCO<sub>3</sub> (3.2 mM/1.0 mM) buffer solution was used as eluent and the anionic suppressor was H<sub>2</sub>SO<sub>4</sub> (100 mM).

## 3. Results and discussion

### 3.1. Characterization

Fig. 1 shows the XRD patterns of the as-prepared NH<sub>2</sub>-MIL-125, g-

Table 1

Experimental and theoretical (in parentheses) elemental analysis.

Photocatalyst	C (%)	H (%)	N (%)
25%C <sub>3</sub> N <sub>4</sub>	31.7 (36.0)	4.1 (1.6)	19.3 (19.0)
50%C <sub>3</sub> N <sub>4</sub>	33.6 (37.0)	3.2 (1.0)	35.9 (33.0)
75%C <sub>3</sub> N <sub>4</sub>	35.5 (38.0)	2.8 (0.5)	49.1 (47.0)

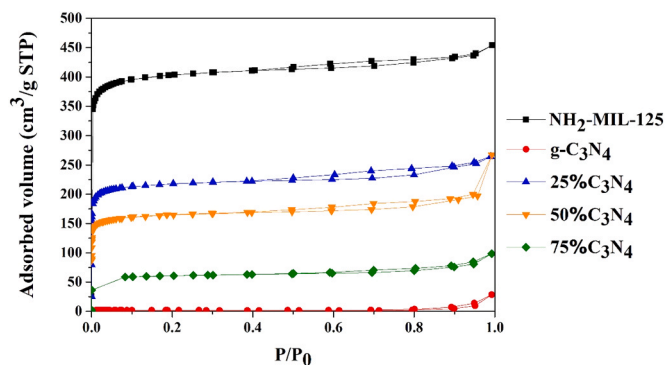


Fig. 2. Nitrogen adsorption-desorption isotherms of the bare semiconductors and the synthesized hybrid materials.

C<sub>3</sub>N<sub>4</sub> and the hybrid materials prepared. In the case of pure g-C<sub>3</sub>N<sub>4</sub>, broad peaks at 13.0 and 27.6° are observed, corresponding to the (100) and (002) planes of this material, respectively (indicated with circles) (Xu et al., 2017). The peak at 13.0° indexed as the (100) plane is associated to the in-plane structural packing of tri-s-triazine units, with a calculated distance is 0.681 nm corresponding to the hole-to-hole distance in the nitride (Dong et al., 2013). This distance is smaller than that in tri-s-triazine unit (ca. 0.713 nm), probably by the presence of small tilts in the structure of the synthesized g-C<sub>3</sub>N<sub>4</sub> (Wang et al., 2009a, 2009b). The other peak at ca. 27.6° is related to the stacking of aromatic units of g-C<sub>3</sub>N<sub>4</sub> with an interlayer distance of 0.323 nm, corresponding to the (002) plane of the stacking of the conjugated aromatic system. In the case of NH<sub>2</sub>-MIL-125 MOF, the prominent diffraction peaks are observed at 2θ values of 6.8, 9.5 and 11.6° associated with the (101), (200) and (211) planes, respectively (indicated with asterisks) (Kim et al., 2013; Zhu et al., 2016). The diffractogram does not show the characteristic peaks of bulk titanium dioxide phases (anatase and rutile), indicating that the framework of NH<sub>2</sub>-MIL-125 has been successfully crystallized (Wang et al., 2015). It should be mentioned that the intensity of the XRD peaks of NH<sub>2</sub>-MIL-125 is much higher than those of g-C<sub>3</sub>N<sub>4</sub>, which indicates a higher crystallinity of the MOF. This appears clearer in the XRD patterns of 25% and 50%C<sub>3</sub>N<sub>4</sub>, where only those peaks associated to the crystallographic planes of NH<sub>2</sub>-MIL-125 can be clearly observed, with almost absence of the peaks of g-C<sub>3</sub>N<sub>4</sub>. In the case of the 75%C<sub>3</sub>N<sub>4</sub> sample, the diffraction peaks of both g-C<sub>3</sub>N<sub>4</sub> and NH<sub>2</sub>-MIL-125 are observed due to the significantly higher proportion of the former. It can be concluded that, under the conditions of the synthesis, the crystalline structure of both semiconductors does not suffer significant modifications. Table 1 summarizes the experimental and theoretical (in parentheses) elemental analysis of 25%C<sub>3</sub>N<sub>4</sub>, 50%C<sub>3</sub>N<sub>4</sub> and 75%C<sub>3</sub>N<sub>4</sub>. The theoretical percentages were calculated according to their elemental formulation of g-C<sub>3</sub>N<sub>4</sub> (39.1% C; 60.9%N) and NH<sub>2</sub>-MIL-125 (34.9% C; 2.1%H; 5.1% N) and the proportion of the two components used in the preparation of the mixtures. In general terms, the experimental and theoretical values fit quite well, confirming the proportion of g-C<sub>3</sub>N<sub>4</sub> and NH<sub>2</sub>-MIL-125 in the hybrid materials.

N<sub>2</sub> adsorption-desorption at -196 °C was employed to characterized the textural properties of these materials, being the resulting isotherms depicted in Fig. 2. NH<sub>2</sub>-MIL-125 MOF yielded a type I-like isotherm with a small hysteresis loop, thus, indicating an essentially microporous

**Table 2**

Textural properties and values of the band gap of all materials and the pseudo-first-order rate constant of DCF degradation.

	$S_{\text{BET}}$ (m <sup>2</sup> /g)	$S_{\text{ext}}$ (m <sup>2</sup> /g)	$V_{\text{M}}$ (cm <sup>3</sup> /g)	$V_{\text{T}}$ (cm <sup>3</sup> /g)	$E_{\text{g}}$ (eV)	$k$ (min <sup>-1</sup> )
NH <sub>2</sub> -MIL-125	1308	102	0.58	0.70	2.56	0.0108
g-C <sub>3</sub> N <sub>4</sub>	5.4	–	0.004	0.04	2.68	0.0066
25% C <sub>3</sub> N <sub>4</sub>	707	63	0.31	0.41	2.60	0.0138
50% C <sub>3</sub> N <sub>4</sub>	536	56	0.23	0.40	2.56	0.0282
75% C <sub>3</sub> N <sub>4</sub>	188	28	0.08	0.15	2.58	0.0194

$S_{\text{BET}}$ , BET surface area;  $S_{\text{ext}}$ , non-microporous surface area;  $V_{\text{MP}}$  and  $V_{\text{T}}$ , micropore and total pore volume, respectively;  $E_{\text{g}}$ , bandgap;  $k$ , kinetic constant.

structure with some contribution of mesoporosity (Fan et al., 2018). In contrast, g-C<sub>3</sub>N<sub>4</sub> showed almost negligible N<sub>2</sub> adsorption except some small amount at high relative pressures, suggesting a fairly scarce mesoporosity in a basically non-porous solid (Zhang et al., 2017). As expected, the samples resulting from hybrids of both materials correlates well with the proportions of NH<sub>2</sub>-MIL-125 and g-C<sub>3</sub>N<sub>4</sub>, showing a higher porosity as the relative amount of MOF increases, being that porosity of the same character. Despite this, it should be mentioned that the reduction in the amount of N<sub>2</sub> adsorbed does not follow a linear trend with the proportion of both components, suggesting that g-C<sub>3</sub>N<sub>4</sub> may partially block MOF pores. Table 2 collects the data of the porous texture of the samples. NH<sub>2</sub>-MIL-125 gave a BET surface area, pore volume and micropore volume very similar to the reported in previous studies (Kim et al., 2013; Martis et al., 2014; Rada et al., 2015). In contrast, the external area value was higher (Gómez-Avilés et al., 2019), which can be related to the additional washings carried out in the synthesis, allowing more efficient removal of trapped solvent molecules. In the case of g-C<sub>3</sub>N<sub>4</sub>, the values obtained are in agreement with the previously given in the literature (Lima et al., 2017; Liu et al., 2017; Zhao et al., 2015a, 2015b). The textural parameters of the hybrids are in the expected values depending on the MOF/g-C<sub>3</sub>N<sub>4</sub> ratio. Increasing g-C<sub>3</sub>N<sub>4</sub> content causes the blockage of the MOF pores, decreasing the surface area and porosity.

Fig. 3A and B represent the UV-Vis absorption spectra and the derived Tauc plots of the different samples, respectively. The bare NH<sub>2</sub>-MIL-125 spectrum shows two absorption bands, with maxima around

280 and 390 nm. The charge transfer from O to Ti (LMCT=ligand-to-metal charge transfer) in the (Ti<sub>8</sub>O<sub>8</sub>(OH)<sub>4</sub>) metal clusters is associated with the band at 280 nm, whereas the second absorption band is related to transferring charges from the amino groups to the (Ti<sub>8</sub>O<sub>8</sub>(OH)<sub>4</sub>) clusters through the organic linker. This broad absorption in the visible-light region results in the characteristic yellow colour of this MOF (Gómez-Avilés et al., 2019; Huang et al., 2020). Regarding the bare g-C<sub>3</sub>N<sub>4</sub>, its characteristic bands appeared in the 350–380 nm range and are associated with  $\pi$ - $\pi^*$  transitions of conjugated ring system (Pannari et al., 2017). Yan et al. (2009) concluded that the absorption edges of the g-C<sub>3</sub>N<sub>4</sub> synthesized from melamine shifted significantly to longer wavelengths at increasing synthesis temperature. This behaviour is probably due to the higher number of defects in the structure. The defects are related to the alterations in the regular structural order of g-C<sub>3</sub>N<sub>4</sub>, usually associated to the synthesis performed at high temperatures, such as the destruction of the connected  $\pi$ -conjugated system (Yan et al., 2009). These defects can result in a reduction of the mobility of the charges, and thus reduce their recombination rate, resulting in an increase of the photoactivity (Gu et al., 2015). In the current study, we used a relatively high temperature for the synthesis of g-C<sub>3</sub>N<sub>4</sub> (550 °C), which can justify the broad absorption observed in the visible light range. Further, a significantly stronger absorption can be observed in the visible range (specifically, 450–800 nm) in the hybrid materials. This behaviour, previously reported in the literature for NH<sub>2</sub>-MIL-125 @g-C<sub>3</sub>N<sub>4</sub> composites (Tian et al., 2018), can be ascribed to the close contact between the particles of the two components, which would facilitate the charge transfer between both semiconductors, thus, enhancing the light absorption and resulting in the observed red-shift of the adsorption edge. It should be mentioned that this absorption band is close to the wavelength of the LED irradiation (384 nm) that will be used in the photocatalytic degradation tests. The bandgap values ( $E_{\text{g}}$ ) are collected in Table 2. NH<sub>2</sub>-MIL-125 yielded a value of 2.56 eV, similar to those already reported (Hendon et al., 2013; Wang et al., 2019a, 2019b), and g-C<sub>3</sub>N<sub>4</sub> displayed a band gap of 2.68 eV, also similar to the reported in the literature (Lima et al., 2017; Martínez et al., 2011; Xiao et al., 2019). The bandgap values of the hybrids were 2.60, 2.56 and 2.58 eV for 25%C<sub>3</sub>N<sub>4</sub>, 50%C<sub>3</sub>N<sub>4</sub> and 75%C<sub>3</sub>N<sub>4</sub>, respectively. These  $E_{\text{g}}$  values are close to the pristine MOF, suggesting that this last is the determining component regarding the optical properties of the hybrid samples (Yi

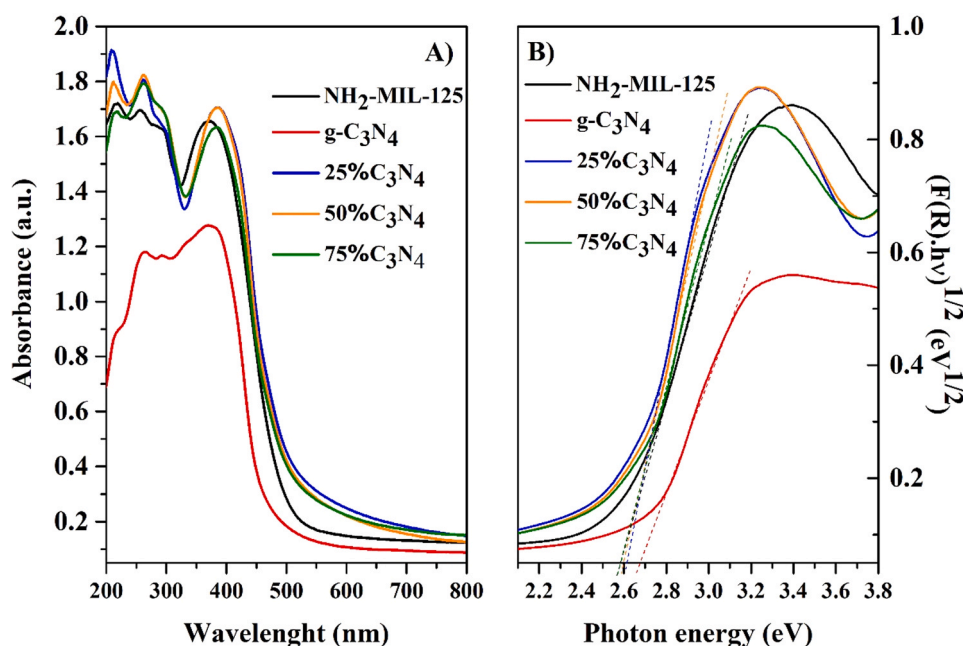


Fig. 3. (A) UV-vis absorption spectra and (B) Tauc plots of the hybrid materials synthesized.



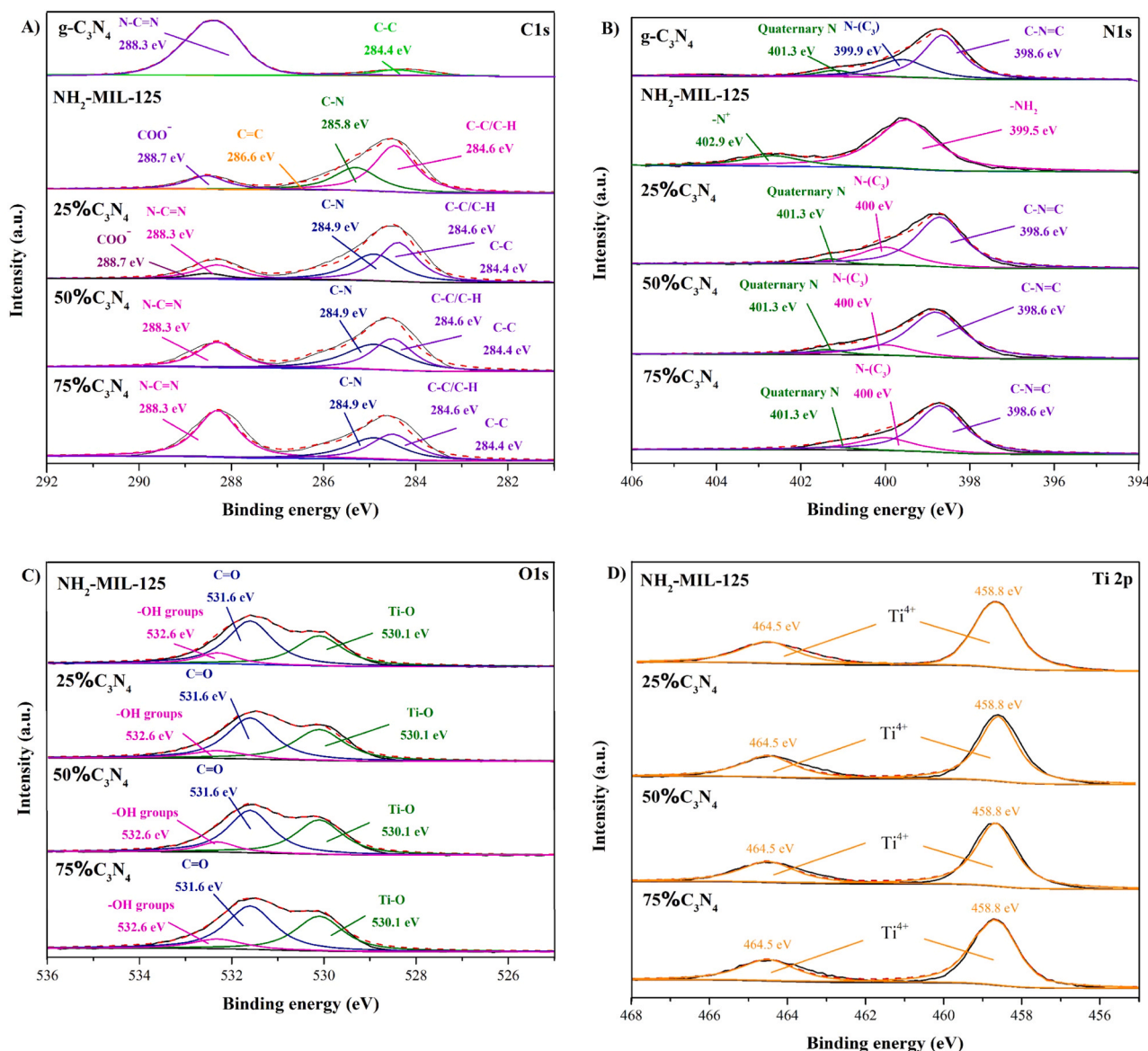


Fig. 4. XPS spectra A) C 1s, B) N 1s, C) O 1s and D) Ti 2p.

et al., 2019).

The surface composition of the materials was analysed by XPS analysis. In the case of  $\text{NH}_2\text{-MIL-125}$ , four peaks are identified in the C 1s spectrum (Fig. 4A). The peaks at 284.6, 285.8, 286.6 and 288.7 eV correspond to C-C/C-H, C-N, C=C and  $\text{COO}^-$ , respectively. In the case of the N 1s spectrum (Fig. 4B), this signal is deconvoluted using two peaks located at 399.5 and 402.9 eV corresponding to amine group, and  $\text{N}^+$ , respectively (Wang et al., 2015). Three peaks are identified in the O 1s spectrum (Fig. 4C), related to Ti-O, C=O and -OH groups at 530.1, 531.6 and 532.6 eV, respectively. Finally, Ti 2p spectrum (Fig. 4D) presents two peaks at 464.5 and 458.8 eV, corresponding to the  $\text{Ti}^{4+}$  ions of the metal oxo-clusters that constituted this MOF (Wang et al., 2018). On the other hand,  $\text{g-C}_3\text{N}_4$  C 1s spectrum (Fig. 4A) shows two peaks, one at 288.3 eV related to the presence of  $\text{N-C}\equiv\text{N}$ , and the second peak at 284.4 eV associated to C-C bonds of  $\text{g-C}_3\text{N}_4$ . The N 1s of carbon nitride spectrum (Fig. 4B) presents three peaks associated to the presence of (i) quaternary N bonded three carbon atoms at 401.3 eV, (ii)  $\text{N-(C}_3\text{)}$  units at 399.9 eV, and (iii) C-N=C in the triazine rings at 398.6 eV. In the case of the C 1s spectra of the hybrid samples (Fig. 4A) three peaks are observed. The first peak at 288.3 eV corresponded to  $\text{N-C}\equiv\text{N}$ , while C-N bond is identified at 284.9 eV. Then, the peak at 284.6 eV has two

contributions, C-C/C-H from the MOF and C-C from the  $\text{g-C}_3\text{N}_4$  (284.4 eV). Additionally, 25% $\text{C}_3\text{N}_4$  presents other peak at 288.7 eV related to  $\text{COO}^-$  from the MOF due to its major presence in this sample. Moreover, it can be clearly seen that the relative height of the peak at 288.3 eV related to C-N=C increase with the amount of  $\text{g-C}_3\text{N}_4$  in the hybrid sample, in agreement with the high intensity of this peak in the C 1s spectrum of bare  $\text{g-C}_3\text{N}_4$ . On the other hand, three peaks were identified in the N 1s spectra of the hybrids, namely quaternary N,  $\text{N-(C}_3\text{)}$  and C-N=C, located at 401.3, 400 and 398.6 eV, respectively (Ye et al., 2013). These peaks are very similar to those of the pattern  $\text{g-C}_3\text{N}_4$  in agreement with the much higher proportion of nitrogen in the  $\text{g-C}_3\text{N}_4$  moiety. Similarly, the O 1s and Ti 2p spectra of the hybrids are very similar to that of the parent MOF, since  $\text{g-C}_3\text{N}_4$  does not contain oxygen nor titanium. It seems that the bonds are not affected significantly by the different ratios of  $\text{g-C}_3\text{N}_4$  to  $\text{NH}_2\text{-MIL-125}$  used. This was expected since the samples were synthesized by a simple physical mixing at different ratios between  $\text{g-C}_3\text{N}_4$  and  $\text{NH}_2\text{-MIL-125}$ , and thus the formation of new bonds is unlikely.

Fig. 5 shows TEM images of the two semiconductors and the 50%  $\text{C}_3\text{N}_4$  sample.  $\text{NH}_2\text{-MIL-125}$  exhibited plates with rounded edges between 200 and 500 nm particle size, in agreement with previous studies

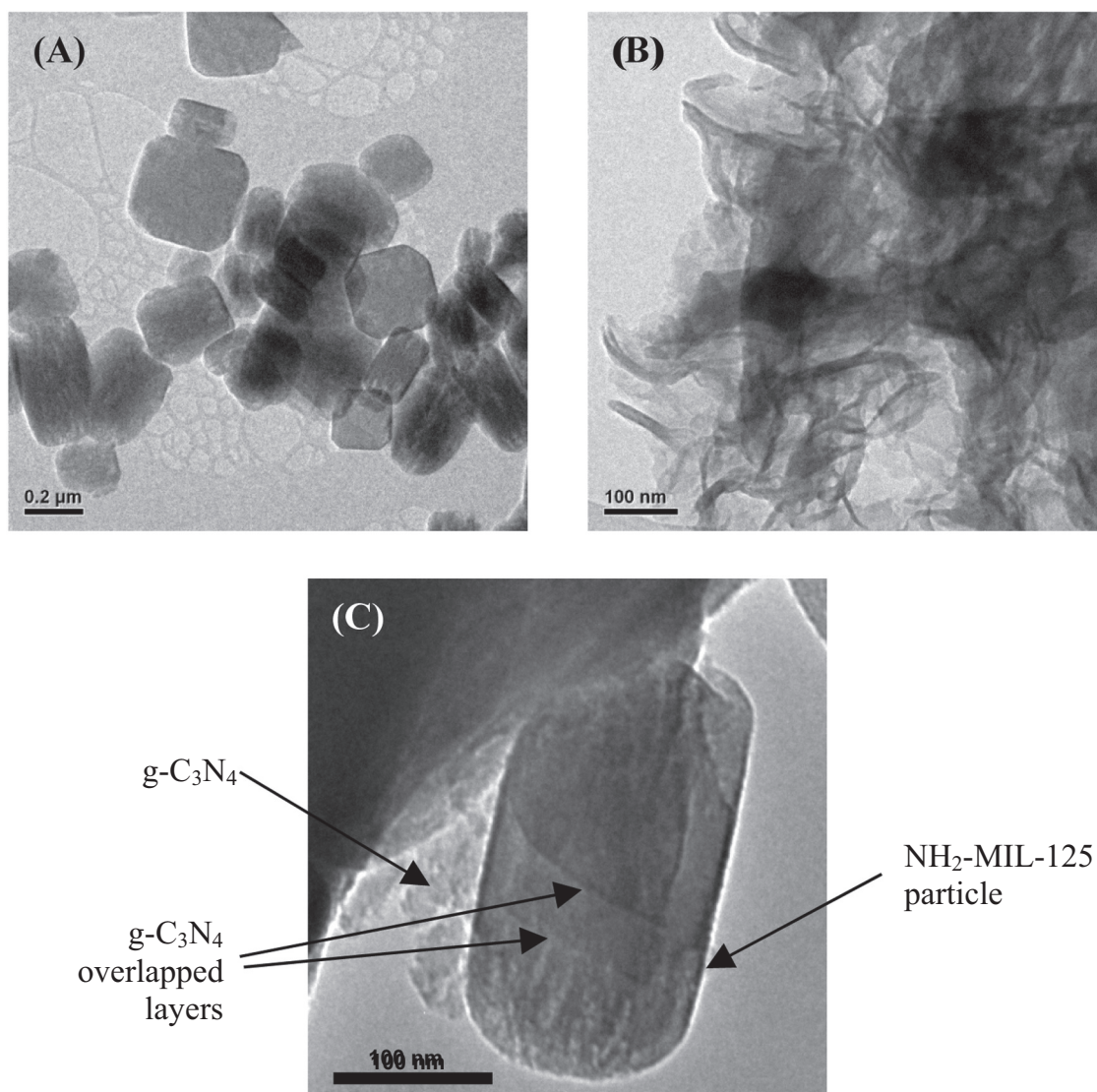


Fig. 5. TEM images of (A)  $\text{NH}_2\text{-MIL-125}$ , (B)  $\text{g-C}_3\text{N}_4$  and (C)  $50\%\text{C}_3\text{N}_4$ .

(Qiu et al., 2019), while  $\text{g-C}_3\text{N}_4$  presented a layered morphology similar to that described previously (Zhang et al., 2016). It can be observed that some of the layers are curled to form some vessels. This inhomogeneity has been attributed to uneven temperature distribution during the synthesis (Li et al., 2009). The  $50\%\text{C}_3\text{N}_4$  sample (Fig. 3C) shows the morphological features of both components in contact between them. Fig. 6 shows the HRTEM image and EDX mapping of C, N, O and Ti from  $50\%\text{C}_3\text{N}_4$ . The HRTEM image (Fig. 6A) shows the presence of several disk-shape particles, associated with MOF particles, below a not so ordered structure that can be probably  $\text{g-C}_3\text{N}_4$ . As can be seen from the EDX mapping results, the elemental distribution fits well with the previous assumptions. The disk-shaped morphologies are mainly composed of Ti, C and O, from the metal nodes ( $\text{Ti}_8\text{O}_8(\text{OH})_4$ ) and the organic linker ( $\text{O}_2\text{C-C}_6\text{H}_3(\text{NH}_2)\text{-CO}_2$ ) of the MOF. Lower amounts of N form also part of this sample, due to the amino group ( $-\text{NH}_2$ ) of the organic linker. On the other hand, the irregular morphology above in the image, is clearly only composed of C and N as corresponds to  $\text{g-C}_3\text{N}_4$  moiety. These images suggest the formation of a hybrid material, which could improve the transfer efficiency and separation of photogenerated charges.

Fig. 7 summarizes the photoluminescence (PL) spectra of the materials synthesized, useful to check the transfer and recombination of photogenerated electron-hole pairs. MOF did not exhibit PL emission in this region with the excitation wavelength used (370 nm). Meanwhile,

the bare  $\text{g-C}_3\text{N}_4$  and the hybrid samples showed two different bands, a more intense one at around 475 nm and another of lower intensity, at 525 nm. The latter corresponds to a radiative recombination of charge carriers captured by traps, while the first one is a result of light emission from direct pairs recombination (Lima et al., 2017). It is accepted that the intensity of the signal is related to the amount of charge recombination. Thus, the greatest relative intensity observed for  $\text{g-C}_3\text{N}_4$  indicates easy recombination of electrons and holes. The hybrid samples yielded weaker PL spectra as the MOF proportion increased, indicating that this component may effectively inhibit the electron-hole recombination. Despite,  $25\%\text{C}_3\text{N}_4$  exhibited the lowest PL intensity among the samples, the PL spectrum of  $50\%\text{C}_3\text{N}_4$  is very similar. Considering the similar PL spectra of both samples seems reasonable predict that the higher activity of the  $50\%\text{C}_3\text{N}_4$  compared with the  $25\%\text{C}_3\text{N}_4$  is not only related with the charge mobility but also to light absorption and interactions with the pollutant molecules.

### 3.2. Photocatalytic tests

The photocatalytic tests of the different samples were checked for the degradation of diclofenac under LED irradiation (384 nm). Before irradiation, all samples were immersed in the diclofenac solution ( $10 \text{ mg}\cdot\text{L}^{-1}$ ) in the dark to achieve the adsorption equilibrium. This reduced the

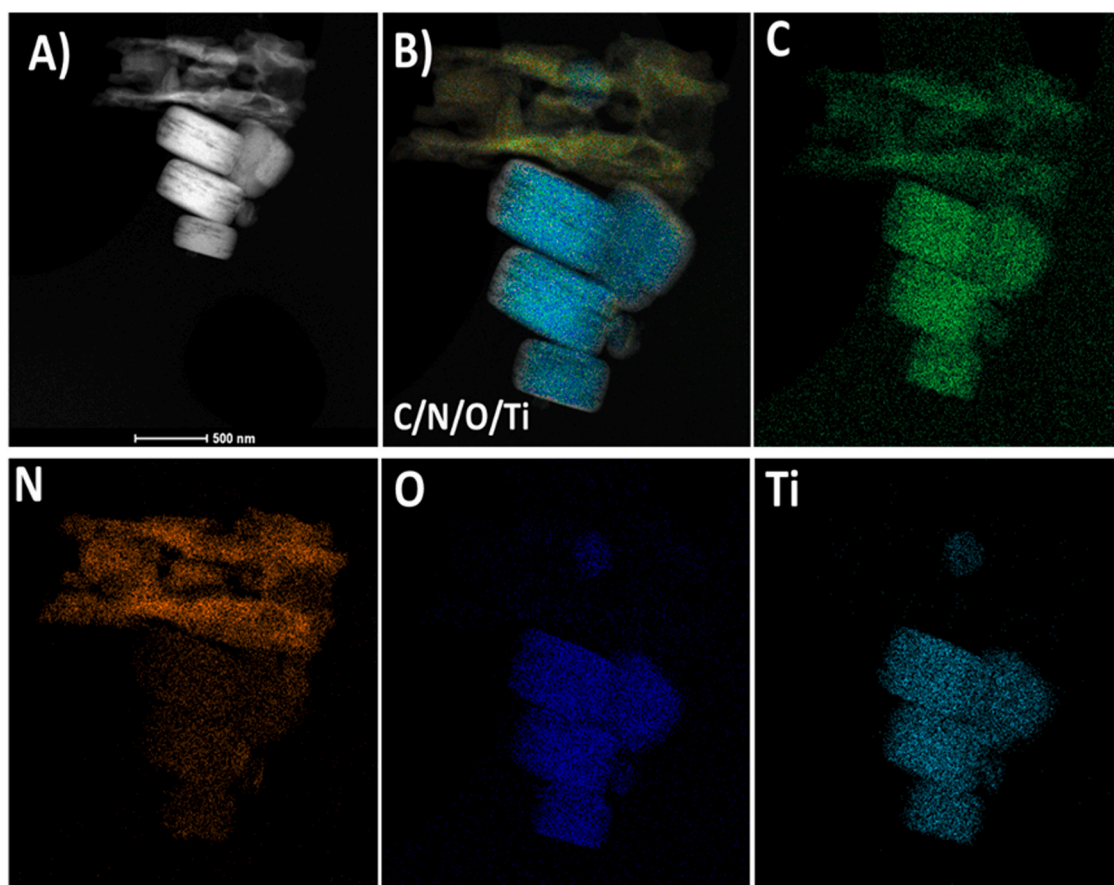


Fig. 6. A) HRTEM image, B) all elements in the same region and EDX element mapping of C, N, O, Ti of 50% $C_3N_4$ .

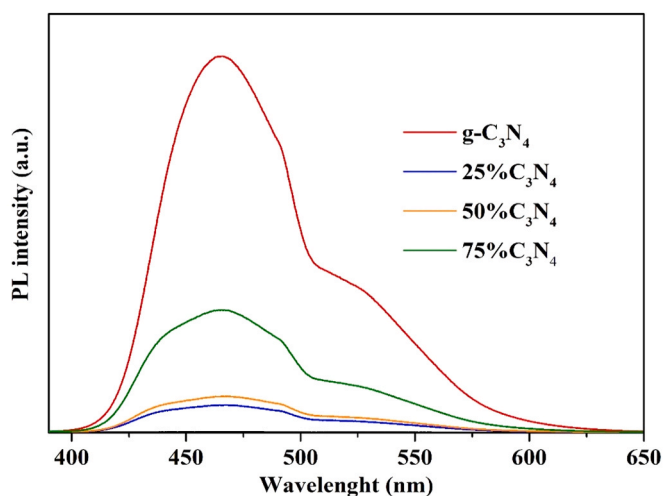


Fig. 7. Photoluminescence spectra of the synthesized hybrid materials compared with the bare  $g-C_3N_4$ .

diclofenac concentration down to ca.  $8 \text{ mg} \cdot \text{L}^{-1}$ , except for  $g-C_3N_4$  that showed negligible adsorption, consistently with its poor porosity. Fig. 8 represents the concentration evolution of diclofenac upon irradiation time with all the materials checked as photocatalysts. Previous blank experiment was carried out, where diclofenac showed negligible degradation, confirming its stability in water under LED irradiation. Neat  $g-C_3N_4$  displayed the lowest photocatalytic performance, achieving only 50% DCF conversion after 2 h of irradiation, while  $NH_2\text{-MIL-125}$  yielded 80% in the same time. Higher photocatalytic degradation rates

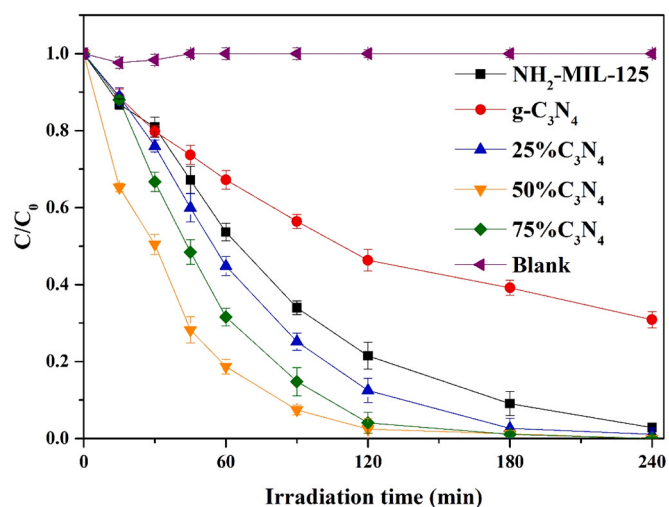


Fig. 8. Evolution of diclofenac concentration upon LED irradiation of all synthesized photocatalysts and the bare semiconductors.

were described by all the hybrid samples, suggesting the occurrence of some synergistic effect associated to the combination of both semiconductors. This enhanced activity can be ascribed to several reasons: (i) a more efficient interfacial charge transfer from  $g-C_3N_4$  to MOF, hence different pathways are provided for the migration of photo-generated charges (Wang et al., 2019a, 2019b; Xu et al., 2017); (ii) a slower recombination rate of these charges as suggested by the PL measurements; and (iii) better light absorption of the hybrids materials as shown



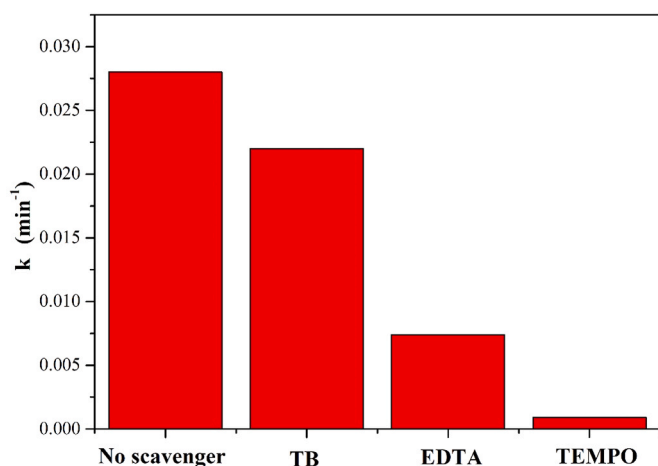


Fig. 9. Effect of EDTA ( $\text{h}^+$ ), TEMPO ( $\text{O}_2^-$ ) and TB ( $\text{HO}^\bullet$ ) scavengers on the rate constant of diclofenac photodegradation for 50% $\text{C}_3\text{N}_4$  (dosage of scavengers = 1 mM).

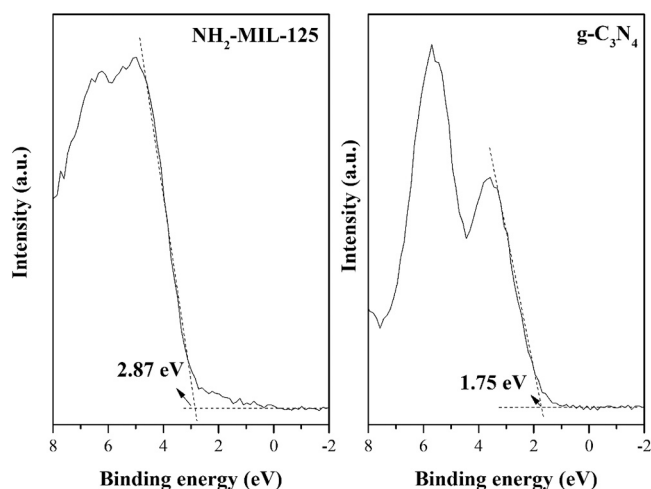


Fig. 10. XPS spectra at low binding energies for the estimation of the maximum valence band (VBM) of (A)  $\text{NH}_2\text{-MIL-125}$  and (B)  $\text{g-C}_3\text{N}_4$ .

by the UV-vis spectra, especially in the case of 50% $\text{C}_3\text{N}_4$ , the one yielding the highest rate of DCF conversion.

According to Calza et al. (2006), the disappearance of diclofenac fits well to a pseudo-first-order rate equation. The values of the rate constant ( $k$ ) are included in Table 2. The highest value, corresponding to 50%  $\text{C}_3\text{N}_4$ , is almost three-fold the one for  $\text{NH}_2\text{-MIL-125}$  and more than four times higher than that of  $\text{g-C}_3\text{N}_4$ . To the best of our knowledge, the literature does not report on the degradation of diclofenac upon UV LED or UV irradiation using MOF/ $\text{g-C}_3\text{N}_4$ . To understand the photocatalytic mechanism occurring during the degradation of DCF several scavengers were used to determine the main species involved in the reaction (Fig. 9). Ethylenediaminetetraacetic acid (EDTA) was used to trap holes ( $\text{h}^+$ ) (Marques et al., 2013; Tao et al., 2015), (2,2,6,6-tetramethylpiperidin-1-yl)oxyl (TEMPO) to trap superoxide radicals (Li et al., 2021), while tert-butanol (TB) was chosen to impair hydroxyl radicals ( $\text{HO}^\bullet$ ) (Jiang et al., 2014; Xu et al., 2011). The corresponding doses (1 mM) were selected on the basis of previous studies (Sampaio et al., 2017; Serpone et al., 2000). EDTA caused major inhibition with almost five-fold decrease of the rate constant. This result evidences the direct contribution of the  $\text{h}^+$  in the photocatalytic removal of DCF under LED irradiation. However, the diclofenac degradation was almost completely inhibited when TEMPO is used, suggesting that superoxide radicals are

the main specie involved in the process. Meanwhile, TB addition caused significantly smaller reduction (around 20%) of the rate constant, indicating that participation of the hydroxyl radicals in the reaction is less important. These results suggest that the active species involved in the photocatalytic mechanism are mainly superoxide radicals, with lower but significant contribution of holes.

The valence band maximum (VBM) of  $\text{g-C}_3\text{N}_4$  and  $\text{NH}_2\text{-MIL-125}$  has been estimated from the XPS, by linear extrapolation of the low binding energy edge of the valence band spectrum (Fig. 10). As can be seen, the VBMs of  $\text{NH}_2\text{-MIL-125}$  and  $\text{g-C}_3\text{N}_4$  are 2.87 and 1.75 eV, respectively. The position of the conduction band (CB) can be approximated from the VBM and band gap values ( $E_{\text{CB}} = \text{VBM} - E_{\text{g}}$ ) resulting in 0.31 and  $-0.93$  eV for  $\text{NH}_2\text{-MIL-125}$  and  $\text{g-C}_3\text{N}_4$ , respectively. According to these results, Fig. 11 depicts a plausible S-scheme photocatalytic mechanism for the degradation of diclofenac (Xu et al., 2020). In this case,  $\text{NH}_2\text{-MIL-125}$  MOF acts as oxidation photocatalyst, while  $\text{g-C}_3\text{N}_4$  acts as reduction photocatalyst. The key to the process is the recombination of the electrons from the conduction band (CB) of the MOF with the holes of the valence band (VB) of  $\text{g-C}_3\text{N}_4$ , avoiding the recombination of the electrons of the CB in  $\text{g-C}_3\text{N}_4$  and the holes in the VB of  $\text{NH}_2\text{-MIL-125}$ , which are those with highest redox ability. This recombination seems to be due to three factors, namely (i) the formation of an internal electric field between both semiconductors, (ii) the band bending produced by the electrons movement, and (iii) the Coulombic attraction between electrons and holes (Xu et al., 2020). The first factor can be explained as follows, when both semiconductors get in contact, the electrons flow spontaneously from  $\text{g-C}_3\text{N}_4$  to the MOF with the formation of an electron depletion layer in  $\text{g-C}_3\text{N}_4$  and an electron accumulation layer in  $\text{NH}_2\text{-MIL-125}$ . Consequently,  $\text{g-C}_3\text{N}_4$  interface is positively charged, while  $\text{NH}_2\text{-MIL-125}$  is negatively charged and an internal electric field from  $\text{g-C}_3\text{N}_4$  to the MOF is formed. This internal electric field accelerates the photogenerated electron transfer from  $\text{NH}_2\text{-MIL-125}$  to  $\text{g-C}_3\text{N}_4$  (in the opposite direction to the internal electric field). The second factor is produced by the Fermi level alignment of both semiconductor when they are in contact. The Fermi level of  $\text{NH}_2\text{-MIL-125}$  undergoes an upward shift, while that of  $\text{g-C}_3\text{N}_4$  suffers a downward shift. These band bendings facilitate the recombination of the electrons in the CB of the MOF and the holes in the VB of  $\text{g-C}_3\text{N}_4$ , with the Coulombic attraction reinforcing the recombination between those electrons and holes. All these processes result in the elimination by recombination of the useless electron and holes. LED irradiation promotes electron transfer from the VB to the CB in both semiconductors, resulting in holes in the respective VB and electrons in the CB. Since the photocatalytic mechanism is mainly due to superoxide radicals with some contribution of holes, it is expected that the electrons located in the CB of the MOF (0.31 eV) migrate to the VB of the  $\text{g-C}_3\text{N}_4$  (1.75 eV), leading to aforementioned recombination. Thus, the electrons in the CB of the  $\text{g-C}_3\text{N}_4$  cannot recombine and can yield superoxide radicals from the oxygen dissolved in the water, since the standard redox potential of  $\text{O}_2/\text{O}_2^{\bullet-}$  ( $-0.33$  eV vs. NHE) is more positive than the CB of this material. As consequence, the holes in the VB of the MOF (2.87 eV) become available for the direct oxidation of the pollutant. The formation of hydroxyl radicals from water by the holes of  $\text{g-C}_3\text{N}_4$  is impeded since the standard redox potential of the  $\text{HO}^\bullet/\text{HO}^-$  (2.40 eV vs. NHE) is more positive than the VB of  $\text{g-C}_3\text{N}_4$ , confirming the lower participation of the  $\text{HO}^\bullet$  radicals in the photocatalytic mechanism. Moreover, the S-scheme favors the charges separation among semiconductors, reducing the recombination rate (as confirmed by PL measurements, Fig. 7).

The stability of the photocatalyst is a crucial issue regarding potential applications. The 50% $\text{C}_3\text{N}_4$  catalyst was characterized after reaction, by  $\text{N}_2$  adsorption-desorption at  $-196^\circ\text{C}$ , XRD and TEM (Fig. 12). The diffraction pattern remained unchanged without additional peaks. The photocatalyst maintains its morphology (plate disks with rounded edges) as suggest the unaltered morphology observed in TEM image. The comparison of the  $\text{N}_2$  adsorption-desorption isotherms of the neat and used MOF shows a slight reduction of the amount of  $\text{N}_2$  adsorbed after



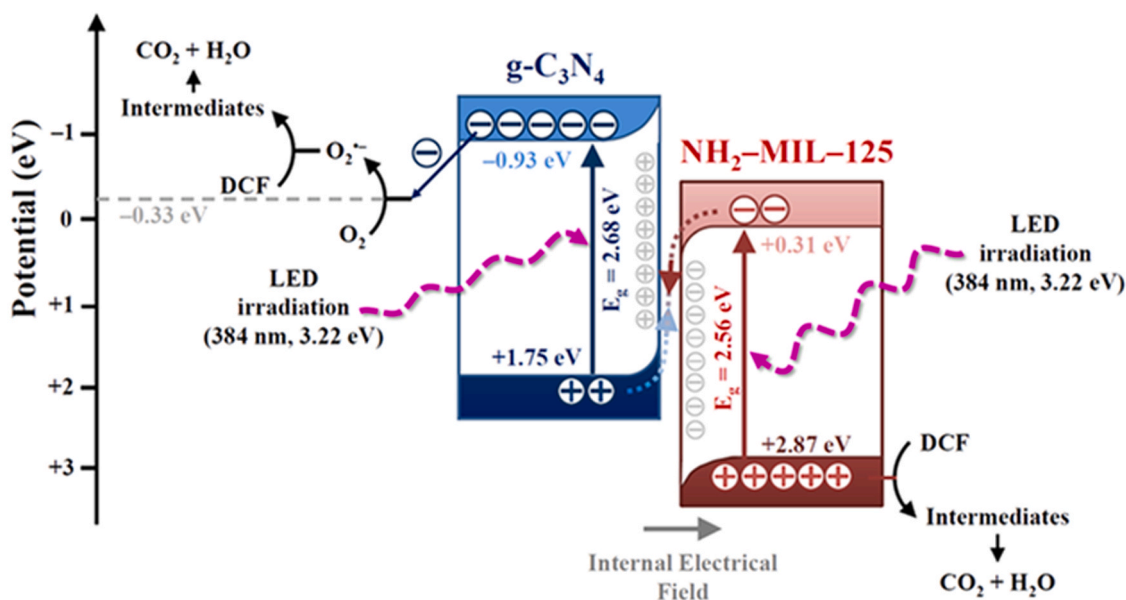


Fig. 11. Proposed S-scheme photocatalytic mechanism for the diclofenac degradation using 50% $\text{C}_3\text{N}_4$ .

use, and consequently, a low-significance decrease of the BET surface area (from 536 to 467  $\text{m}^2\cdot\text{g}^{-1}$ ). This reduction can be associated to the adsorption of diclofenac or reaction by-products at surface of the MOF.

Moreover, TOC mineralization rates are not provided due to a limited but detectable organic linker leaching, as can be observed in a previous study (Gómez-Avilés et al., 2020). Additional effort should be applied to improve the stabilize of this MOF in water.

### 3.3. Reaction by-products and degradation pathway

Table 3 collects the species detected from DCF breakdown with 50%  $\text{C}_3\text{N}_4$ , as measured by LC/ESI-MS and IC. These presented a low mass error ( $\pm 1\text{mDa}$ ) and a correct value of RDB, defined as the amount of rings and double bonds in the molecule. For instance, diclofenac yields 9, being 7 due to double bonds and 2 to the rings. Based on the detected compounds, several degradation pathways are depicted in Fig. 13. In the first route, the C-N cleavage of the side chain can result in the identification of DCF-1 ( $m/z$  161.9872) (Gou et al., 2017). The hydroxylation of this product would give DCF-2 ( $m/z$  177.9821) (Moctezuma et al., 2020). An alternative reaction path was proposed by Zhang et al. (2020) through the decarboxylation of the DCF molecule to give DCF-3\* ( $m/z$  252). Although this intermediate was not detected in our work, its formation may be expected since its oxidized derivative was detected, named DCF-3 ( $m/z$  266.0135). Further hydroxylation of DCF-3 gives the DCF-4 ( $m/z$  282.0085). A third degradation route can begin with the hydroxylation at C5 position of diclofenac, in accordance with previous studies, resulting in the DCF-5 ( $m/z$  312.0184) (Cheng et al., 2015; Lu et al., 2017; Pérez-Estrada et al., 2005). Further oxidation produces DCF-6 ( $m/z$  310.0032) (Calza et al., 2006). In addition, other by-products were detected from the coupling of DCF molecules. First, two DCF molecules would lead to DCF-7 ( $m/z$  589.0252), which upon HCl loss, gives rise to DCF-8 ( $m/z$  553.0486). Formation of dimers has been reported by Keen et al. (2013). Finally, IC analyses showed the formation of short-chain carboxylic acids, such as formic and oxalic, whose evolution can be seen in Fig. 14. The amounts of both acids increased as the reaction proceeded, due to the oxidation of previous by-products. Chloride appeared after 30 min, probably due to the loss of HCl from DCF-7 or some other chlorinated by-products not detected. Only nitrite was detected as mineralization nitrogen product.

## 4. Conclusions

MOF/ $\text{g-C}_3\text{N}_4$  materials to be tested as photocatalysts were successfully synthesized by a straightforward method, using different proportions of both semiconductors. The structure of these two components was observed in all photocatalysts prepared. The porous texture was the result of the highly microporous character of MOF and the non-porous one of  $\text{g-C}_3\text{N}_4$ , although with some lower surface area and pore volume than the expected from the relative amounts of each component, most probably due to partial blockage of the pores by  $\text{g-C}_3\text{N}_4$ . The morphology of the hybrids also showed the main features of both components, including plate-like particles from the MOF and fiber-like from  $\text{g-C}_3\text{N}_4$ . All the MOF/ $\text{g-C}_3\text{N}_4$  samples showed very similar band gap values, closer to the pristine MOF, suggesting that the optical properties are basically determined by this component. These materials have demonstrated photocatalytic activity under LED irradiation, superior to that of the individual components, suggesting the occurrence of some synergistic effect. The MOF presence reduces the electron-holes recombination rate of the  $\text{g-C}_3\text{N}_4$ . Regarding the photocatalytic performance, 50% $\text{C}_3\text{N}_4$  yielded the best result, with complete conversion of the target pollutant (diclofenac) in 2 h, with a pseudo-first-order rate constant value of 0.0282  $\text{min}^{-1}$ , almost three-fold the obtained with the pristine  $\text{NH}_2\text{-MIL-125}$  and more than four-fold the one with  $\text{g-C}_3\text{N}_4$ . Radical trapping experiments proved that superoxide radicals and holes played a significant role in the photocatalytic mechanism. From the reaction species identified, several routes have been proposed for diclofenac degradation pathway, involving, hydroxylation, coupling and oxidation reactions. Short-chain carboxylic acids, such as formic and oxalic acid, were identified as final by-products, as well as chloride and nitrite.

### CRediT authorship contribution statement

V. Muelas-Ramos: Methodology. M.J. Sampaio: Conceptualization, Methodology, Writing - review & editing, Supervision, Funding acquisition. C.G. Silva: Writing - review & editing, Funding acquisition. J. Bedia: Conceptualization, Writing - review & editing, Supervision. J. J. Rodríguez: Writing - review & editing. Supervision, Funding acquisition. J.L. Faria: Conceptualization, Writing - review & editing, Supervision, Funding acquisition. C. Belver: Conceptualization, Writing - review & editing, Supervision, Funding acquisition. All authors have

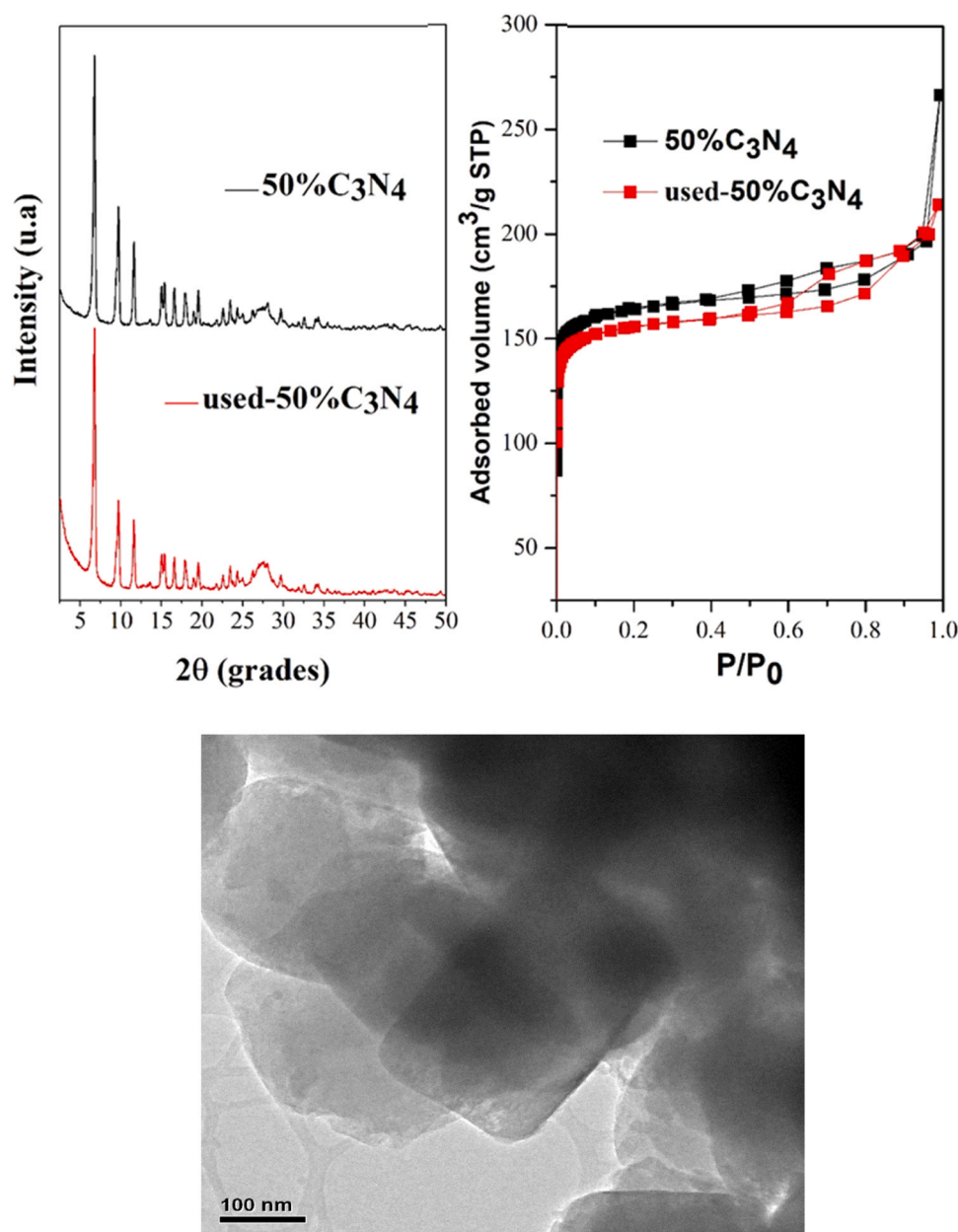


Fig. 12. XRD pattern, nitrogen adsorption-desorption isotherm and TEM image of 50%C<sub>3</sub>N<sub>4</sub> sample after reaction.

Table 3

Accurate mass ( $m/z$ ) values of the species identified in the photocatalytic breakdown of DCF with 50%C<sub>3</sub>N<sub>4</sub>.

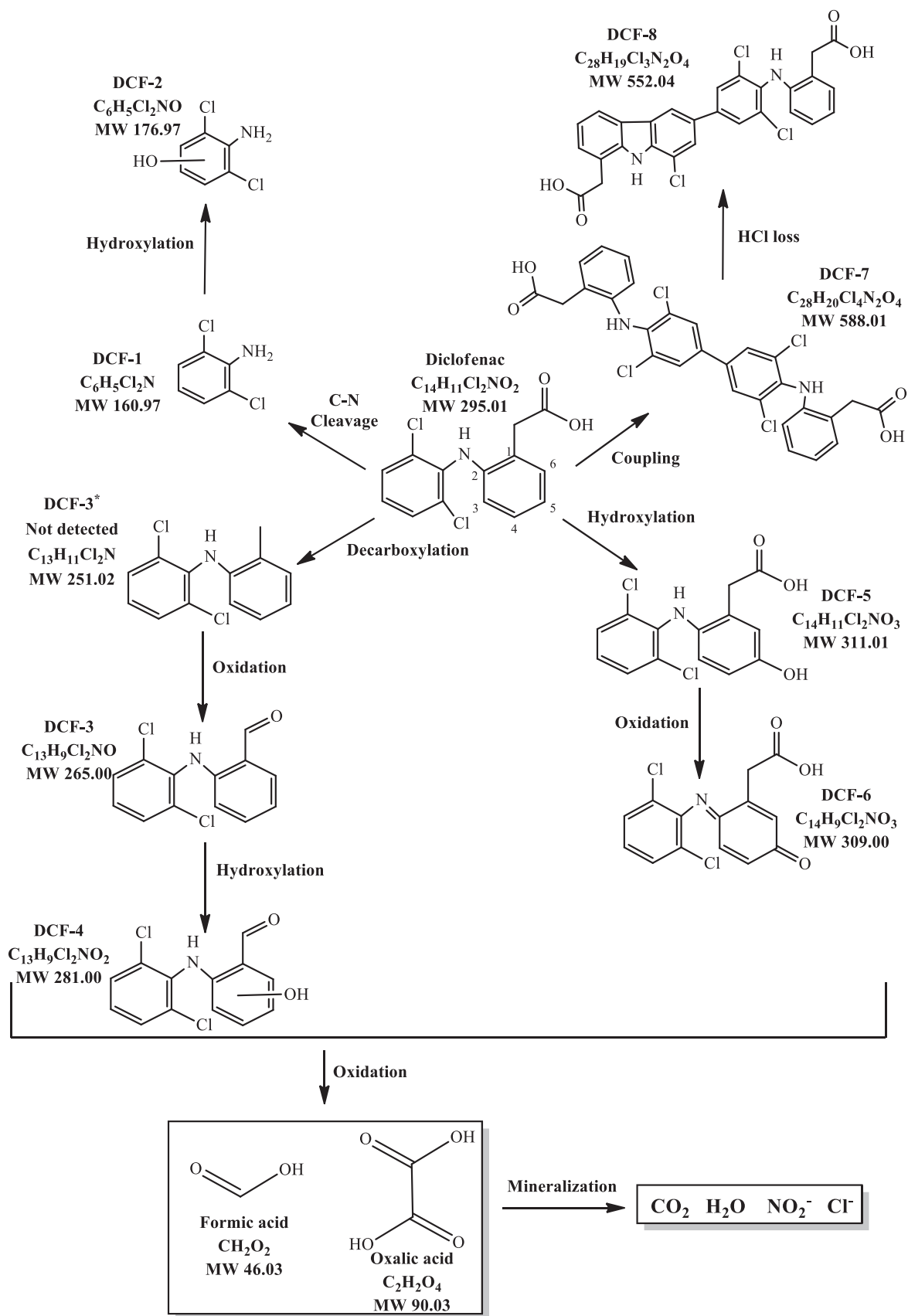
Name	Retention time (min)	Experimental $m/z$ [M + H] <sup>+</sup>	Proposed formula [M + H] <sup>+</sup>	Calculated $m/z$ [M + H] <sup>+</sup>	Mass error (mDa)	Ring Double Bond (RDB)
Diclofenac	17.4	296.0237	C <sub>14</sub> H <sub>12</sub> Cl <sub>2</sub> NO <sub>2</sub>	296.0235	0.9	9
DCF-1	3.2	161.9872	C <sub>6</sub> H <sub>6</sub> Cl <sub>2</sub> N	161.7000	-0.6	4
DCF-2	3.9	177.9821	C <sub>6</sub> H <sub>6</sub> Cl <sub>2</sub> NO	177.9821	-0.1	4
DCF-3	6.9	266.0135	C <sub>13</sub> H <sub>10</sub> Cl <sub>2</sub> NO	266.0134	-0.2	9
DCF-4	8.1	282.0085	C <sub>13</sub> H <sub>10</sub> Cl <sub>2</sub> NO <sub>2</sub>	282.0083	-0.7	9
DCF-5	6.2	312.0184	C <sub>14</sub> H <sub>12</sub> Cl <sub>2</sub> NO <sub>3</sub>	312.0189	0.6	9
DCF-6	6.0	310.0032	C <sub>14</sub> H <sub>10</sub> Cl <sub>2</sub> NO <sub>3</sub>	310.0032	0.1	10
DCF-7	31.9	589.0252	C <sub>28</sub> H <sub>21</sub> Cl <sub>4</sub> N <sub>2</sub> O <sub>4</sub>	589.0266	-0.3	18
DCF-8	30.9	553.0486	C <sub>28</sub> H <sub>20</sub> Cl <sub>3</sub> N <sub>2</sub> O <sub>4</sub>	553.0483	-0.4	19

read and agreed to the published version of the manuscript.

#### Declaration of Competing Interest

The authors declare that they have no known competing financial

interests or personal relationships that could have appeared to influence the work reported in this paper.

Fig. 13. Proposed reaction pathway for DCF photocatalytic breakdown with 50% $C_3N_4$ .



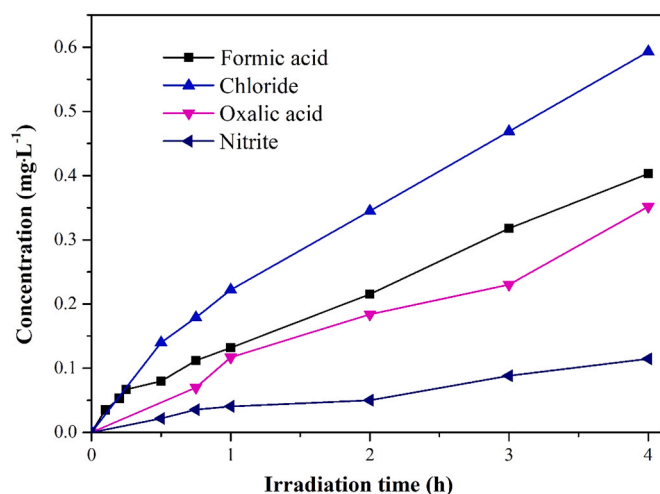


Fig. 14. Evolution of short-chain carboxylic acids, chloride and nitrite concentration upon reaction time with 50% $C_3N_4$ .

## Acknowledgements

This work was financially supported by Associate Laboratory LSRE-LCM - UID/EQU/50020/2020 - funded by national funds through FCT/MCTES (PIDDAC) and by project POCI-01-0145-FEDER-030674, financed by the ERDF through COMPETE2020 and POCI - and by national funds through FCT (Portugal). This research was also funded by Spanish Ministry of Economy and Competitiveness (project CTQ2016-78576-R, FEDER funds) and the State Research Agency (PID2019-106186RB-I00/AEI/10.13039/501100011033) (Spain). V. Muelas-Ramos thanks to MCIU for BES-2017-082613 grant. Authors thank the TEM images from the Centro Nacional de Microscopía Electrónica (Spain). Authors would like to acknowledge the use of Servicio General de Apoyo a la Investigación-SAI for EDX mapping images, Universidad de Zaragoza (Spain) and the Research Support Service of XPS data from University of Málaga (Spain).

## References

- Ahmed, I., Jung, S.H., 2014. Composites of metal-organic frameworks: preparation and application in adsorption. *Mater. Today* 17, 136–146. <https://doi.org/10.1016/j.mat.2014.03.002>.
- Arroyo, P., Molinos-Senante, M., 2018. Selecting appropriate wastewater treatment technologies using a choosing-by-advantages approach. *Sci. Total Environ.* 625, 819–827. <https://doi.org/10.1016/j.scitotenv.2017.12.331>.
- Bahnemann, D., 2004. Photocatalytic water treatment: solar energy applications. *Sol. Energy* 77, 445–459. <https://doi.org/10.1016/j.solener.2004.03.031>.
- Bedia, J., Muelas-Ramos, V., Peñas-Garzón, M., Gómez-Avilés, A., Rodríguez, J., Belver, C., 2019. A review on the synthesis and characterization of metal organic frameworks for photocatalytic water purification. *Catalysts* 9, 52. <https://doi.org/10.3390/catal9010052>.
- Brillas, E., 2020. A review on the photoelectro-Fenton process as efficient electrochemical advanced oxidation for wastewater remediation. Treatment with UV light, sunlight, and coupling with conventional and other photo-assisted advanced technologies. *Chemosphere* 250, 126198. <https://doi.org/10.1016/j.chemosphere.2020.126198>.
- Brunauer, S., Emmett, P.H., Teller, E., 1938. Adsorption of gases in multimolecular layers. *J. Am. Chem. Soc.* 60, 309–319. <https://doi.org/10.1021/ja01269a023>.
- Calza, P., Sakkas, V.A., Medana, C., Baiocchi, C., Dimou, A., Pelizzetti, E., Albanis, T., 2006. Photocatalytic degradation study of diclofenac over aqueous  $TiO_2$  suspensions. *Appl. Catal. B Environ.* 67, 197–205. <https://doi.org/10.1016/j.apcatb.2006.04.021>.
- Cao, S., Low, J., Yu, J., Jaroniec, M., 2015. Polymeric photocatalysts based on graphitic carbon nitride. *Adv. Mater.* 27, 2150–2176. <https://doi.org/10.1002/adma.201500033>.
- Cheng, H., Song, D., Liu, H., Qu, J., 2015. Permanganate oxidation of diclofenac: the pH-dependent reaction kinetics and a ring-opening mechanism. *Chemosphere* 136, 297–304. <https://doi.org/10.1016/j.chemosphere.2014.11.062>.
- Dong, F., Zhao, Z., Xiong, T., Ni, Z., Zhang, W., Sun, Y., Ho, W.K., 2013. In situ construction of  $g-C_3N_4/g-C_3N_4$  metal-free heterojunction for enhanced visible-light photocatalysis. *ACS Appl. Mater. Interfaces* 5, 11392–11401. <https://doi.org/10.1021/am403653a>.
- Fan, Y.H., Zhang, S.W., Qin, S., Bin, Li, X.S., Qi, S.H., 2018. An enhanced adsorption of organic dyes onto  $NH_2$  functionalization titanium-based metal-organic frameworks and the mechanism investigation. *Microporous Mesoporous Mater.* 263, 120–127. <https://doi.org/10.1016/j.micromeso.2017.12.016>.
- Fu, Y., Sun, L., Yang, H., Xu, L., Zhang, F., Zhu, W., 2016. Visible-light-induced aerobic photocatalytic oxidation of aromatic alcohols to aldehydes over Ni-doped  $NH_2$ -MIL-125( $Ti$ ). *Appl. Catal. B Environ.* 187, 212–217. <https://doi.org/10.1016/j.apcatb.2016.01.038>.
- Gómez-Avilés, A., Peñas-Garzón, M., Bedia, J., Dionysiou, D.D., Rodríguez, J.J., Belver, C., 2019. Mixed Ti-Zr metal-organic-frameworks for the photodegradation of acetaminophen under solar irradiation. *Appl. Catal. B Environ.* 253, 253–262. <https://doi.org/10.1016/j.apcatb.2019.04.040>.
- Gómez-Avilés, A., Muelas-Ramos, V., Bedia, J., Rodríguez, J.J., Belver, C., 2020. Thermal post-treatments to enhance the water stability of  $NH_2$ -MIL-125( $Ti$ ). *Catalysts* 10, 603. <https://doi.org/10.3390/catal10060603>.
- Gou, J., Ma, Q., Cui, Y., Deng, X., Zhang, H., Cheng, X., Li, X., Xie, M., Cheng, Q., Liu, H., 2017. Visible light photocatalytic removal performance and mechanism of diclofenac degradation by  $Ag_3PO_4$  sub-microcrystals through response surface methodology. *J. Ind. Eng. Chem.* 49, 112–121. <https://doi.org/10.1016/j.jiec.2017.01.015>.
- Gu, Q., Gao, Z., Zhao, H., Lou, Z., Liao, Y., Xue, C., 2015. Temperature-controlled morphology evolution of graphitic carbon nitride nanostructures and their photocatalytic activities under visible light. *RSC Adv.* 5, 49317–49325. <https://doi.org/10.1039/c5ra07284k>.
- Hendon, C.H., Tiana, D., Fontecave, M., Sanchez, C., D'arras, L., Sasso, C., Rozes, L., Mellot-Draznics, C., Walsh, A., 2013. Engineering the optical response of the titanium-MIL-125 metal-organic framework through ligand functionalization. *J. Am. Chem. Soc.* 135, 10942–10945. <https://doi.org/10.1021/ja405350u>.
- Huang, H., Wang, X.S., Philo, D., Ichihara, F., Song, H., Li, Y., Li, D., Qiu, T., Wang, S., Ye, J., 2020. Toward visible-light-assisted photocatalytic nitrogen fixation: a titanium metal organic framework with functionalized ligands. *Appl. Catal. B Environ.* 267, 118686. <https://doi.org/10.1016/j.apcatb.2020.118686>.
- Jiang, Y., Wang, W.N., Biswas, P., Fortner, J.D., 2014. Facile aerosol synthesis and characterization of ternary crumpled graphene- $TiO_2$ -magnetite nanocomposites for advanced water treatment. *ACS Appl. Mater. Interfaces* 6, 11766–11774. <https://doi.org/10.1021/am5025275>.
- Jiménez, S., Micó, M.M., Arnaldos, M., Medina, F., Contreras, S., 2018. State of the art of produced water treatment. *Chemosphere* 192, 186–208. <https://doi.org/10.1016/j.chemosphere.2017.10.139>.
- Kampouri, S., Ireland, C.P., Valizadeh, B., Oveisi, E., Schouwink, P.A., Mensi, M., Stylianou, K.C., 2018. Mixed-phase MOF-derived titanium dioxide for photocatalytic hydrogen evolution: the impact of the templated morphology. *ACS Appl. Energy Mater.* 1, 6541–6548. <https://doi.org/10.1021/acsaem.8b01445>.
- Kanakaraju, D., Glass, B.D., Oelgemöller, M., 2018. Advanced oxidation process-mediated removal of pharmaceuticals from water: a review. *J. Environ. Manag.* 219, 189–207. <https://doi.org/10.1016/j.jenvman.2018.04.103>.
- Keen, O.S., Thurman, E.M., Ferrer, I., Dotson, A.D., Linden, K.G., 2013. Dimer formation during UV photolysis of diclofenac. *Chemosphere* 93, 1948–1956. <https://doi.org/10.1016/j.chemosphere.2013.06.079>.
- Kim, S.-N., Kim, J., Kim, H.-Y., Cho, H.-Y., Ahn, W.-S., 2013. Adsorption/catalytic properties of MIL-125 and  $NH_2$ -MIL-125. *Catal. Today* 204, 85–93. <https://doi.org/10.1016/j.cattod.2012.08.014>.
- Li, D., Liu, H., Niu, C., Yuan, J., Xu, F., 2019. Mpg- $C_3N_4$ -ZIF-8 composites for the degradation of tetracycline hydrochloride using visible light. *Water Sci. Technol.* 80, 2206–2217. <https://doi.org/10.2166/wst.2020.038>.
- Li, D., Huang, J., Li, R., Chen, P., Chen, D., Cai, M., Liu, H., Feng, Y., Lv, W., Liu, G., 2021. Synthesis of a carbon dots modified  $g-C_3N_4/SnO_2$  Z-scheme photocatalyst with superior photocatalytic activity for PPCPs degradation under visible light irradiation. *J. Hazard. Mater.* 401, 123257. <https://doi.org/10.1016/j.jhazmat.2020.123257>.
- Li, X., Zhang, J., Shen, L., Ma, Y., Lei, W., Cui, Q., Zou, G., 2009. Preparation and characterization of graphitic carbon nitride through pyrolysis of melamine. *Appl. Phys. A Mater. Sci. Process.* 94, 387–392. <https://doi.org/10.1007/s00339-008-4816-4>.
- Li, Y., Fang, Y., Cao, Z., Li, N., Chen, D., Xu, Q., Lu, J., 2019. Construction of  $g-C_3N_4/PDI@MOF$  heterojunctions for the highly efficient visible light-driven degradation of pharmaceutical and phenolic micropollutants. *Appl. Catal. B Environ.* 250, 150–162. <https://doi.org/10.1016/j.apcatb.2019.03.024>.
- Liang, S., Zhang, D., Pu, X., Yao, X., Han, R., Yin, J., Ren, X., 2019. A novel  $Ag_2O/g-C_3N_4$  p-n heterojunction photocatalysts with enhanced visible and near-infrared light activity. *Sep. Purif. Technol.* 210, 786–797. <https://doi.org/10.1016/j.seppur.2018.09.008>.
- Lima, M.J., Silva, A.M.T., Silva, C.G., Faria, J.L., 2017. Graphitic carbon nitride modified by thermal, chemical and mechanical processes as metal-free photocatalyst for the selective synthesis of benzaldehyde from benzyl alcohol. *J. Catal.* 353, 44–53. <https://doi.org/10.1016/j.jcat.2017.06.030>.
- Lippens, B.C., de Boer, J.H., 1965. Studies on pore systems in catalysts. *J. Catal.* 4, 319–323. [https://doi.org/10.1016/0021-9517\(65\)90307-6](https://doi.org/10.1016/0021-9517(65)90307-6). V. t Method.
- Liu, S., Chen, F., Li, S., Peng, X., Xiong, Y., 2017. Enhanced photocatalytic conversion of greenhouse gas  $CO_2$  into solar fuels over  $g-C_3N_4$  nanotubes with decorated transparent ZIF-8 nanoclusters. *Appl. Catal. B Environ.* 211, 1–10. <https://doi.org/10.1016/j.apcatb.2017.04.009>.
- Lu, X., Shao, Y., Gao, N., Chen, J., Zhang, Y., Xiang, H., Guo, Y., 2017. Degradation of diclofenac by UV-activated persulfate process: kinetic studies, degradation pathways and toxicity assessments. *Ecotoxicol. Environ. Saf.* 141, 139–147. <https://doi.org/10.1016/j.ecoenv.2017.03.022>.

- Marques, R.R.N., Sampaio, M.J., Carrapiço, P.M., Silva, C.G., Morales-Torres, S., Dražić, G., Faria, J.L., Silva, A.M.T., 2013. Photocatalytic degradation of caffeine: developing solutions for emerging pollutants. *Catal. Today* 209, 108–115. <https://doi.org/10.1016/j.cattod.2012.10.008>.
- Martínez, C., Canle, L., Fernández, M., Santaballa, M.I., Faria, J. J.A., 2011. Aqueous degradation of diclofenac by heterogeneous photocatalysis using nanostructured materials. *Appl. Catal. B Environ.* 107, 110–118. <https://doi.org/10.1016/j.apcatb.2011.07.003>.
- Martis, M., Meicheng, W., Mori, K., Yamashita, H., 2014. Fabrication of metal nanoparticles in metal organic framework NH<sub>2</sub>-MIL-125 by UV photo-assisted methods for optimized catalytic properties. *Catal. Today* 235, 98–102. <https://doi.org/10.1016/j.cattod.2014.02.046>.
- Miklos, D.B., Remy, C., Jekel, M., Linden, K.G., Drewes, J.E., Hübner, U., 2018. Evaluation of advanced oxidation processes for water and wastewater treatment – a critical review. *Water Res.* 139, 118–131. <https://doi.org/10.1016/j.watres.2018.03.042>.
- Moctezuma, E., Leyva, E., Lara-Pérez, C., Noriega, S., Martínez-Richa, A., 2020. TiO<sub>2</sub> photocatalytic degradation of diclofenac: intermediates and total reaction mechanism. *Top. Catal.* 63, 601–615. <https://doi.org/10.1007/s11244-020-01262-7>.
- Panneri, S., Minju Thomas, A., Priyanka Ganguly, A., Nair, B.N., Peer Mohamed, cd A., K Warrier, K.G., Hareesh, U.S., 2017. C<sub>3</sub>N<sub>4</sub> anchored ZIF 8 composites: photo-regenerable, high capacity sorbents as adsorptive photocatalysts for the effective removal of tetracycline from water. *Catal. Sci. Technol.* 7, 2118–2128. <https://doi.org/10.1039/c7cy00348j>.
- Pérez-Estrada, L.A., Malato, S., Gernjak, W., Agüera, A., Thurman, E.M., Ferrer, I., Fernández-Alba, A.R., 2005. Photo-fenton degradation of diclofenac: Identification of main intermediates and degradation pathway. *Environ. Sci. Technol.* 39, 8300–8306. <https://doi.org/10.1021/es050794n>.
- Qiu, J., Yang, L., Li, M., Yao, J., 2019. Metal nanoparticles decorated MIL-125-NH<sub>2</sub> and MIL-125 for efficient photocatalysis. *Mater. Res. Bull.* 112, 297–306. <https://doi.org/10.1016/j.matresbull.2018.12.038>.
- Rada, Z.H., Abid, H.R., Shang, J., He, Y., Webley, P., Liu, S., Sun, H., Wang, S., 2015. Effects of amino functionality on uptake of CO<sub>2</sub>, CH<sub>4</sub> and selectivity of CO<sub>2</sub>/CH<sub>4</sub> on titanium based MOFs. *Fuel* 160, 318–327. <https://doi.org/10.1016/j.fuel.2015.07.088>.
- Salimi, M., Esrafil, A., Jafari, A.J., Gholami, M., Sobhi, H.R., 2020. Application of MIL-53(Fe)/urchin-like g-C<sub>3</sub>N<sub>4</sub> nanocomposite for efficient degradation of cefixime. *Inorg. Chem. Commun.* 111, 107565 <https://doi.org/10.1016/j.inoche.2019.107565>.
- Sampaio, M.J., Lima, M.J., Baptista, D.L., Silva, A.M.T., Silva, C.G., Faria, J.L., 2017. Ag-loaded ZnO materials for photocatalytic water treatment. *Chem. Eng. J.* 318, 95–102. <https://doi.org/10.1016/j.cej.2016.05.105>.
- Serpone, N., Texier, I., Emeline, A.V., Pichat, P., Hidaka, H., Zhao, J., 2000. Post-irradiation effect and reductive dechlorination of chlorophenols at oxygen-free TiO<sub>2</sub>/water interfaces in the presence of prominent hole scavengers. *J. Photochem. Photobiol. A Chem.* 136, 145–155. [https://doi.org/10.1016/S1010-6030\(00\)00348-8](https://doi.org/10.1016/S1010-6030(00)00348-8).
- Song, K., Mohseni, M., Taghipour, F., 2016. Application of ultraviolet light-emitting diodes (UV-LEDs) for water disinfection: a review. *Water Res.* 94, 341–349. <https://doi.org/10.1016/j.watres.2016.03.003>.
- Tao, H., Liang, X., Zhang, Q., Chang, C.T., 2015. Enhanced photoactivity of graphene/titanium dioxide nanotubes for removal of Acetaminophen. *Appl. Surf. Sci.* 324, 258–264. <https://doi.org/10.1016/j.apsusc.2014.10.129>.
- Tauc, J., 1970. Absorption edge and internal electric fields in amorphous semiconductors. *Mater. Res. Bull.* 5, 721–729. [https://doi.org/10.1016/0025-5408\(70\)90112-1](https://doi.org/10.1016/0025-5408(70)90112-1).
- Tian, X., Zhou, M., Tan, C., Li, M., Liang, L., Li, K., Su, P., 2018. KOH activated N-doped novel carbon aerogel as efficient metal-free oxygen reduction catalyst for microbial fuel cells. *Chem. Eng. J.* 348, 775–785. <https://doi.org/10.1016/j.cej.2018.05.007>.
- UNESCO/HELCOM, 2017. Pharmaceuticals in the Aquatic Environment of the Baltic Sea region – A status report. UNESCO Emerging Pollutants in Water Series – No. 1. UNESCO Publishing, Paris.
- Wang, C.C., Yi, X.H., Wang, P., 2019b. Powerful combination of MOFs and C<sub>3</sub>N<sub>4</sub> for enhanced photocatalytic performance. *Appl. Catal. B Environ.* 247, 24–48. <https://doi.org/10.1016/j.apcatb.2019.01.091>.
- Wang, H., Yuan, X., Wu, Y., Zeng, G., Chen, X., Leng, L., Wu, Z., Jiang, L., Li, H., 2015. Facile synthesis of amino-functionalized titanium metal-organic frameworks and their superior visible-light photocatalytic activity for Cr(VI) reduction. *J. Hazard. Mater.* 286, 187–194. <https://doi.org/10.1016/J.JHAZMAT.2014.11.039>.
- Wang, H., Cui, P.H., Shi, J.X., Tan, J.Y., Zhang, J.Y., Zhang, N., Zhang, C., 2019a. Controllable self-assembly of CdS@NH<sub>2</sub>-MIL-125(Ti) heterostructure with enhanced photodegradation efficiency for organic pollutants through synergistic effect. *Mater. Sci. Semicond. Process.* 97, 91–100. <https://doi.org/10.1016/j.mssp.2019.03.016>.
- Wang, M., Yang, L., Yuan, J., He, L., Song, Y., Zhang, H., Zhang, Z., Fang, S., 2018. Heterostructured Bi<sub>2</sub>S<sub>3</sub>@NH<sub>2</sub>-MIL-125(Ti) nanocomposite as a bifunctional photocatalyst for Cr(VI) reduction and rhodamine B degradation under visible light. *RSC Adv.* 8, 12459–12470. <https://doi.org/10.1039/c8ra00882e>.
- Wang, X., Chen, X., Thomas, A., Fu, X., Antonietti, M., 2009a. Metal-Containing Carbon Nitride Compounds: A New Functional Organic-Metal Hybrid Material. *Adv. Mater.* 21, 1609–1612. <https://doi.org/10.1002/adma.200802627>.
- Wang, X., Maeda, K., Thomas, A., Takanabe, K., Xin, G., Carlsson, J.M., Domen, K., Antonietti, M., 2009b. A metal-free polymeric photocatalyst for hydrogen production from water under visible light. *Nat. Mater.* 8, 76–80. <https://doi.org/10.1038/nmat2317>.
- Wen, J., Xie, J., Chen, X., Li, X., 2017. A review on g-C<sub>3</sub>N<sub>4</sub> -based photocatalysts. *Appl. Surf. Sci.* 391, 72–123. <https://doi.org/10.1016/j.apsusc.2016.07.030>.
- Xiao, N., Li, S., Liu, S., Xu, B., Li, Y., Gao, Y., Ge, L., Lu, G., 2019. Novel PtPd alloy nanoparticle-decorated g-C<sub>3</sub>N<sub>4</sub> nanosheets with enhanced photocatalytic activity for H<sub>2</sub> evolution under visible light irradiation. *Cuihua Xuebao Chin. J. Catal.* 40, 352–361. [https://doi.org/10.1016/S1872-2067\(18\)63180-8](https://doi.org/10.1016/S1872-2067(18)63180-8).
- Xu, J., Gao, J., Wang, C., Yang, Y., Wang, L., 2017. NH<sub>2</sub>-MIL-125(Ti)/graphitic carbon nitride heterostructure decorated with NiPd co-catalysts for efficient photocatalytic hydrogen production. *Appl. Catal. B Environ.* 219, 101–108. <https://doi.org/10.1016/j.apcatb.2017.07.046>.
- Xu, Q., Zhang, L., Cheng, B., Fan, J., Yuj, 2020. S-scheme heterojunction photocatalyst. *Chem* 6, 1–17. <https://doi.org/10.1016/j.chempr.2020.06.010>.
- Xu, T., Zhang, L., Cheng, H., Zhu, Y., 2011. Significantly enhanced photocatalytic performance of ZnO via graphene hybridization and the mechanism study. *Appl. Catal. B Environ.* 101, 382–387. <https://doi.org/10.1016/j.apcatb.2010.10.007>.
- Yan, S.C., Li, Z.S., Zou, Z.G., 2009. Photodegradation performance of g-C<sub>3</sub>N<sub>4</sub> fabricated by directly heating melamine. *Langmuir* 25, 10397–10401. <https://doi.org/10.1021/la900923z>.
- Yi, X.H., Ma, S.Q., Du, X.D., Zhao, C., Fu, H., Wang, P., Wang, C.C., 2019. The facile fabrication of 2D/3D Z-scheme g-C<sub>3</sub>N<sub>4</sub>/UiO-66 heterojunction with enhanced photocatalytic Cr(VI) reduction performance under white light. *Chem. Eng. J.* 375, 121944 <https://doi.org/10.1016/j.cej.2019.121944>.
- Zeng, Y., Liu, C., Wang, L., Zhang, S., Ding, Y., Xu, Y., Liu, Y., Luo, S., 2016. A three-dimensional graphitic carbon nitride belt network for enhanced visible light photocatalytic hydrogen evolution. *J. Mater. Chem. A* 4, 19003–19010. <https://doi.org/10.1039/C6TA07397B>.
- Zhang, L., He, X., Xu, X., Liu, C., Duan, Y., Hou, L., Zhou, Q., Ma, C., Yang, X., Liu, R., Yang, F., Cui, L., Xu, C., Li, Y., 2017. Highly active TiO<sub>2</sub>/g-C<sub>3</sub>N<sub>4</sub>/G photocatalyst with extended spectral response towards selective reduction of nitrobenzene. *Appl. Catal. B Environ.* 203, 1–8. <https://doi.org/10.1016/j.apcatb.2016.10.003>.
- Zhang, L., Liu, Y., Fu, Y., 2020. Degradation kinetics and mechanism of diclofenac by UV/peracetic acid. *RSC Adv.* 10, 9907–9916. <https://doi.org/10.1039/d0ra00363h>.
- Zhang, T., Zhao, D., Wang, Y., Chang, Y., Zhang, D., Tang, Y., Pu, X., Shao, X., 2019. Facial synthesis of a novel Ag<sub>4</sub>V<sub>2</sub>O<sub>7</sub>/g-C<sub>3</sub>N<sub>4</sub> heterostructure with highly efficient photoactivity. *J. Am. Ceram. Soc.* 102, 3897–3907. <https://doi.org/10.1111/jace.16254>.
- Zhang, W., Zhou, L., Deng, H., 2016. Ag modified g-C<sub>3</sub>N<sub>4</sub> composites with enhanced visible-light photocatalytic activity for diclofenac degradation. *J. Mol. Catal. A Chem.* 423, 270–276. <https://doi.org/10.1016/j.molcata.2016.07.021>.
- Zhao, H.M., Di, C.M., Wang, L., Chun, Y., Xu, Q.H., 2015a. Synthesis of mesoporous graphitic C<sub>3</sub>N<sub>4</sub> using cross-linked bimodal mesoporous SBA-15 as a hard template. *Microporous Mesoporous Mater.* 208, 98–104. <https://doi.org/10.1016/j.micromeso.2015.01.047>.
- Zhao, Z., Sun, Y., Dong, F., 2015b. Graphitic carbon nitride based nanocomposites: a review. *Nanoscale* 7, 15–37. <https://doi.org/10.1039/c4nr03008g>.
- Zhou, Z., Qiu, L., Wang, J., Pang, J., Yang, F., Yang, Y., Duo, S., 2019. Photocatalysts Fabricated by Depositing Ag on Co-g-C<sub>3</sub>N<sub>4</sub> and Its Enhanced Visible-Light Photocatalytic Performance. *IOP Conference Series: Materials Science and Engineering* 678, 012126. <https://doi.org/10.1088/1757-899X/678/1/012126>.
- Zhu, S.-R., Liu, P.-F., Wu, M.-K., Zhao, W.-N., Li, G.-C., Tao, K., Yi, F.-Y., Han, L., 2016. Enhanced photocatalytic performance of BiOBr/NH<sub>2</sub>-MIL-125(Ti) composite for dye degradation under visible light. *Dalton Trans.* 45, 17521–17529. <https://doi.org/10.1039/C6DT02912D>.